

THE FLORIDA STATE UNIVERSITY
COLLEGE OF ARTS AND SCIENCES

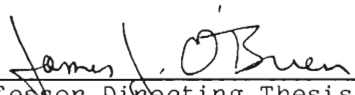
THE WIND DRIVEN SEASONAL CIRCULATION
IN THE SOUTHERN TROPICAL INDIAN OCEAN

by


KAREN E. WOODBERRY

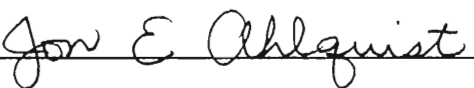
A Thesis submitted to the
Department of Meteorology
in partial fulfillment of the
requirements for the degree of
Master of Science

Approved:



Professor Directing Thesis





Spring, 1988

Spring, 1988

Abstract

The FSU Indian Ocean model, driven by the climatological mean winds of Hellerman and Rosenstein (1983), accurately simulates the major features of the large scale upper ocean circulation observed in the Southern Hemisphere and equatorial regions. The principal feature in the tropical Indian Ocean is a basin-wide clockwise (cyclonic) gyre comprised of the South Equatorial Current to the south, the South Equatorial Counter Current to the north, and the East African Coastal Current in the west. Rossby waves propagate westward in the shear zone between the South Equatorial Current and the South Equatorial Counter Current, and are obstructed and partially reflected by the banks along the Seychelles-Mauritius Ridge (60°E). A region of high eddy activity northwest of Madagascar is an extension of the tropical gyre and appears to be a tropical analog to the Gulf Stream recirculation region. Oscillations in meridional transport at the equator have westward phase speed and eastward group velocity and may be either mixed Rossby-gravity (Yanai) waves or short Rossby waves. Frequencies and wavelengths in the model solutions indicate the region of the equatorial dispersion curves where these two types of waves can be easily confused.

Oscillations with 30-60 day periods are seen in most currents. These oscillations cannot be atmospherically forced as the shortest period in the mean monthly wind forcing is 60 days. These oscillations cannot be atmospherically forced as the shortest period in the mean monthly wind forcing is 60 days.

Mean transports in the western basin agree well with observations. Small (0.4 Sv) mean throughflow at the eastern boundary due to wind forced Indian Ocean dynamics alone is toward the Pacific in conflict with observations of throughflow from the Pacific.

Acknowledgements

I am grateful to my advisor Dr. James J. O'Brien for believing in my abilities and for supporting and guiding me through my degree. Dr. Mark Luther provided invaluable assistance in the course of this work. My thanks go to Mr. David Legler and Mr. Jim Merritt for their computer assistance. I thank Dr. Jon Ahlquist and Dr. Sharon Nicholson for serving on my committee. Mrs. Rita Kuyper cheerfully deciphered and made numerous corrections to this manuscript and I am grateful for her expertise and encouragement.

Most of this work was done while I was supported by a NASA Traineeship in Physical Oceanography and Meteorology. Additional support for this work was provided by the Office of Naval Research through the Secretary of the Navy Chair in Oceanography and the Institute of Naval Oceanography. Computing resources were provided by the FSU Computing Center. The wind analysis was supported by the NOAA TOGA project office.

Numerous colleagues, friends, and family provided academic assistance and emotional support in the past two and a half years and this would not have been possible without them.

Table of Contents

	PAGE
List of Tables.....	vi
List of Figures.....	vii
List of Abbreviations.....	xx
I. Introduction.....	1
II. The Model.....	8
III. Wind Forcing.....	14
IV. Results.....	22
1. Large scale circulation.....	22
2. SEC branch transports.....	45
3. Eastern boundary throughflow.....	60
4. Transport variability.....	63
5. Mozambique Channel.....	70
6. Leeuwin Current.....	73
V. Discussion.....	76
References.....	81

List of Tables

	PAGE
Table 1. Transport in SEC branch currents. Locations are marked in Fig. 3. Oscillations are present in a higher frequency range than is resolved by the mean monthly wind forcing.....	47
Table 2. Comparison of Madagascar boundary current transports with transports from data calculations and Kindle reduced gravity model.....	59

List of Figures

	PAGE
Fig. 1: Number of observations, N, from 1870 to 1976 per 2° latitude x 2° longitude box, smoothed; light shading for N < 50, no shading for 50 < N < 500 and dark shading for N > 500. From Hellerman and Rosenstein (1983).....	2
Fig. 2: Observed large scale surface circulation during NE and SW monsoons. From Pickard and Emery (1982).....	5
Fig. 3: Model geometry following the 200m depth contour. Land boundaries are shaded. This study focuses on the region south of 5°N. Islands in this region are identified in the text. Transect locations correspond to Table 1.....	10
Fig. 4: Staggered grid used in finite difference approximation, showing relative location of U, V and H points. J is the index in the zonal (ϕ) direction and K is the meridional (θ) index.....	12
Fig. 5: Wind stress for January 16 during the NE monsoon. Vectors are wind stress direction and magnitude (see scale on Somali peninsula). Contour interval is $.01 \text{ N m}^{-2}$. Winds over	

the South China Sea are not used by the model. Strongest winds are found in the southeast trades between 20°S and 25°S, 85°E to 95°E. Monsoon winds are maximum on either side of 5°N near the African coast. Northeasterly winds are also found east of India. Winds at the eastern boundary are westward..... 15

Fig. 6: Wind stress curl for January 16 during the NE monsoon. Contour interval is $2 \times 10^{-8} \text{ Nm}^{-3}$. Labels are in units of 10^{-9} Nm^{-3} . Curl fields have been smoothed both zonally and meridionally with a single 1-2-1 Hanning filter. A band of strong negative curl extends across the basin between 5°-10°S and 20°S. There is negative curl along western Australia, in the Mozambique Channel and along the Somali Coast. Strong positive curl is found in the region of the southern subtropical gyre. A band of strong positive curl between 10°N and 5°S extends south along the African coast into the northern Mozambique Channel..... 15

Fig. 7: Wind stress as in Fig. 5 for May 16 at the beginning of the SW monsoon. Strongest winds are still in the southeasterly trades. The tradewinds extend across the equator with southwesterly flow along the Somali Coast. Strong winds in the Bay of Bengal are also southwesterly. Westerly winds are seen at the equator with easterly winds at the eastern in the Bay of Bengal are also southwesterly. Westerly winds are seen at the equator with easterly winds at the eastern

boundary..... 16

Fig. 8: Wind stress curl as in Fig. 6 for May 16 at the beginning of the SW monsoon. Strong negative curl from 5°N to 15°S, in the northern Arabian Sea and Bay of Bengal, and in the Mozambique Channel. Strong positive curl south of 15°S, along the Somali and Omani coasts and around the tip of India..... 16

Fig. 9: Wind stress as in Fig. 5 for July 16 at the height of the SW monsoon. Contour interval is .04 Nm⁻². Maximum southwesterlies are found over the Arabian Sea with weaker southwesterlies in the Bay of Bengal. The southeast trades are nearing peak strength and coverage (August). Easterly winds at the western boundary..... 17

Fig. 10: Wind stress curl as in Fig. 6 for July 16 at the height of the SE monsoon. Contour interval is 4×10^{-8} Nm⁻³. The overall pattern seen in May has intensified with sharp gradients between regions of strongly positive and negative curl. Positive curl in the south extends around the tip of Madagascar and northward along the African coast. Negative curl covers the interior of the domain..... 17

Fig. 11: Wind stress as in Fig. 5 for October 16 during the SW

Fig. 11: Wind stress as in Fig. 5 for October 16 during the SW

to NE monsoon transition. Southeast trades are still strong, extending to the African coast. Northern Hemisphere winds are weak with northerly winds appearing in the northern Arabian Sea. A jet of westerly winds is centered at 5°N, 85°E. Weak winds at the eastern boundary changing to westerly..... 18

Fig. 12: Wind stress curl as in Fig. 6 for October 16 during the SW to NE monsoon transition. Strong positive curl across the south to 15°S with strong negative curl to the equator. The biggest changes since July are found in the northwest where there is a mixture of weak positive and negative curl with stronger negative curl appearing in the far north. Curl at the African coast is still positive. The region of positive curl around India has spread and weakened since July..... 18

Fig. 13: Model velocity vectors and upper layer thickness contours in the SW quadrant of the domain. Velocity scale vector in the upper left. Contour scale in meters along the bottom. The large island 45°-50°E is Madagascar with the Farquhar group of islands to the northeast. Saya de Malha and Nazareth Banks are at 60°E..... 23

a) February 4. Annual Rossby wave near 10°S, 70°E in SEC-SECC shear zone is beginning to "feel" the blocking of the Seychelles-Mauritius Ridge. The wave from the previous year
Seychelles-Mauritius Ridge. The wave from the previous year

has contracted to a small eddy passing between the banks at 60°E. The subtropical gyre is seen at the southern boundary. Anticyclonic circulation in the northern Mozambique Channel..... 23

b) June 27. Rossby wave contracting, moving south east of the Seychelles-Mauritius Ridge. Strong high pressure cell in the northern Mozambique Channel..... 23

c) November 24. Oscillations in SEC due to Rossby wave propagation and blocking at 60°E. Recirculation due to eddy activity west of the Farquhar Islands. Trough in Mozambique Channel extends almost to 20°S..... 23

Fig. 14: Meridional transport at 13°S. Transect cuts through the Rossby wave zone from 55° to 120°E. a) Longitude-time contours. One year of data is repeated three times to show the propagation of the Rossby wave. Solid (dashed) contours indicate northward (southward) flow. A single Rossby wave is generated each year near 110°E which has a westward phase speed of 9.3 cm s^{-1} as measured from the center of the figure. Transport is in Sverdrups ($10^6 \text{ m}^3 \text{ s}^{-1}$) with a contour interval of .1 Sv. b) Annual cycle. Net transport at this latitude is northward (positive) December through March and southward (negative) April through November. The strong annual signal indicates an annual Rossby wave. There are hints of oscillations with a period of about 36 days. The curve has

been smoothed with a single pass of a 1-2-1 Hanning filter..... 26

Fig. 15: As in Fig. 13 for the NW quadrant of the domain.

Note the two velocity scales. Cape Amber at the tip of Madagascar is just visible at 49°E. Other "land" regions are the Farquhar Islands NE of Cape Amber; the Seychelles at 15°S, 55°E; Saya de Malha Bank at 61°E; the Chagos Archipelago at 7°S, 72°E; and the Maldives and Gan along 73°E..... 28

a) January 19. EACC and Somali Current meet and turn offshore near 3°S. Flow meanders eastward through the islands to feed the SECC with strongest flow between 6°S and 10°S. Equatorial currents are westward. Equatorial Rossby waves visible at 4°N and 4°S near 50°E..... 28

b) May 10. Eddy activity between the equator and 10°S is discussed in the text. Outflow from the region now includes strong eastward flow at the equator. Eastward transport is increasing ULT in the east..... 28

c) August 22. The "southern gyre" just south of the equator has spun off a clockwise eddy into the Northern Hemisphere. Meridional velocities are prominent at the equator during this transition to eastward flow..... 29

d) November 15. Eddies bracketing the equator are moving south under the influence of the NE monsoon. Outflow from their convergence zone evidences strong cross equatorial south under the influence of the NE monsoon. Outflow from their convergence zone evidences strong cross equatorial

oscillations. Equatorial currents are beginning to reverse in the east..... 29

Fig. 16: Eddy kinetic energy (EKE) for one year in the equatorial region near the African coast, 40° - 80°E, 5°N - 12°S. EKE is concentrated at the coast south of the equator with a maximum of $280 \times 10^{-4} \text{ m}^2\text{s}^{-2}$ near 3°S. Zonal relative maxima are separated by approximately 250km. Labels are in units of $10^{-4} \text{ m}^2\text{s}^{-2}$ with a contour interval of $1.0 \times 10^{-3} \text{ m}^2\text{s}^{-2}$ 31

Fig. 17: Longitude-time contours of zonal transport at the equator. Solid (dashed) contours indicate eastward (westward) transport. Between 60°E and 90°E flow is predominantly eastward in February through early June and August through mid-November. Maxima occur in the western basin. Transitions occur generally from east to west except in August. Transport is in Sverdrups ($10^6 \text{ m}^3\text{s}^{-1}$) with a contour interval of .3 Sv..... 35

Fig. 18: As in Fig. 13 for the NE quadrant of the domain. Indonesia is in the NE corner..... 37

a) March 9. Eastward equatorial currents and associated downwelling Kelvin waves increase the ULT at the eastern boundary. Coastal Kelvin waves propagate along the Indonesian downwelling Kelvin waves increase the ULT at the eastern boundary. Coastal Kelvin waves propagate along the Indonesian

coast..... 37

b) May 18. Equatorial current splits near 80°E. South of the equator the flow appears geostrophic (along ULT contours) and feeds the SECC. The northern flow continues eastward with large cross equatorial oscillations seen near 90°E as currents begin to reverse to westward..... 37

c) July 2. Strong westward flow at equator down the east-west pressure gradient..... 38

d) September 26. Equatorial currents have split near 75°E with the southern flow remaining near the equator longer. The ULT gradient is sharper in the north and currents are stronger... 38

Fig. 19. Same as Fig. 13 for SE quadrant of domain. Australia is in the lower right corner with Indonesia in the upper right... 41

a) March 5. Several Rossby waves are visible in the SEC-SECC shear zone near 14°S. The SECC does not appear as a continuous zonal flow but rather as a number of tributaries feeding in north of successive Rossby waves. A ridge in the thermocline is present at 110°E with southward flow at the Australian coast..... 41

b) August 28. Rossby waves slanted NW-SE in the west. SECC more continuous over this region at this time. A trough in the thermocline near Australia causes northward flow along the coast..... 41

thermocline near Australia causes northward flow along the coast..... 41

Fig. 20: Schematic diagram of the large scale Southern Hemisphere and equatorial circulation discussed in the text. Double-ended arrows indicate currents which reverse during the year. Current names can be found in the list of abbreviations... 43

Fig. 21: Zonal transport in the SEC and Rossby wave zone at 63°E. a) Latitude-time contours for 8° - 20°S. Solid (dashed) lines show eastward (westward) transport. The shallow banks along the Seychelles-Mauritius Ridge are located just west of this transect at 60°E. The SECC is seen north of 10°S. Transport units are Sverdrups ($10^6 \text{ m}^3 \text{ s}^{-1}$); contour interval is .1 Sv. b) Total westward transport in the SEC at 63°E, 10° - 23°S. The annual Rossby wave dominates the seasonal cycle..... 48

Fig. 22: Latitude-time contours of zonal transport across 53°E in the band 11°S - 21°S. Solid (dashed) contours denote eastward (westward) flow. The two branches of the SEC impinging on the coast of Madagascar are visible at 11° - 15°S and 17° - 21°S. Maxima in the northern branch occur in January through February and July through October. The southern branch shows maximum transport in September through January. Some slight eastward flow is observed in the shadow of the shallow banks of the Seychelles-Mauritius Ridge at 60°E. Transport is slight eastward flow is observed in the shadow of the shallow banks of the Seychelles-Mauritius Ridge at 60°E. Transport is

in Sverdrups ($10^6 \text{ m}^3\text{s}^{-1}$) with a contour interval of .1 Sv..... 49

Fig. 23: Meridional transport at 12°S . a) Longitude-time contours from 50°E to 60°E . Solid (dashed) lines indicate northward (southward) transport. Rossby wave trapped east of the Seychelles-Mauritius Ridge at 60°E is seen to propagate westward as an eddy until it is absorbed into the northward current. There is no apparent seasonal cycle in the strong current close to the coast. Transport is in Sverdrups ($10^6 \text{ m}^3\text{s}^{-1}$) with contour interval of .2 Sv. b) Smoothed (single pass of 1-2-1 Hanning) annual cycle between 50°E and 53°E . This includes most of the flow that rounds the tip of Madagascar. Mean transport is 11.3 Sv. with seasonal range of 4.3 Sv..... 51

Fig. 24: Meridional transport in East Madagascar Current and Northeast Madagascar Current. Mean northward transport at 16°S , $50^\circ - 52^\circ\text{E}$ is 8.1 Sv. Seasonal cycle shows a maximum in May and a minimum in September. Mean southward transport at 22°S , $48^\circ - 50^\circ\text{E}$ is 8.2 Sv. Seasonal cycle shows maxima in November - December and a minimum in late April. Seasonal range in both currents is about 3.5 Sv or about 40% of the mean flow. Both transects have been smoothed using a single pass of a 1-2-1 Hanning filter. Note that current transports are out-flow. Both transects have been smoothed using a single pass of a 1-2-1 Hanning filter. Note that current transports are out-

of-phase in their seasonal cycles but in-phase at a higher frequency (approximate period of 30-33 days)..... 52

Fig. 25: Meridional transport at 19°S. a) Longitude-time contours for 49° - 60°E. Solid (dashed) contours indicate northward (southward) flow. Southward flow at 50°E is the EMC. Transport units are Sverdrups ($10^6 \text{ m}^3\text{s}^{-1}$) with a contour interval of .06 Sv. b) Annual cycle of total transport across 19°S. Positive (negative) values indicate northward (southward) transport. Solid curve is transport between 49°E and 60°E which includes the EMC. Mean transport is .7 Sv with maximum northward flow in March - May and southward flow seen only in mid-July to mid-September. Oscillations have a period of about 40 days. Dashed curve is transport between 51°E and 60°E which excludes the EMC. A similar seasonal cycle is evident with a mean transport of 1.4 Sv. The oscillations are absent. Both curves have been smoothed with a single pass of a 1-2-1 Hanning filter..... 54

Fig. 26: Westward transport at 49°E, 10°S - 11.6°S. a) Latitude-time contours. The blank area of the figure is the tip of Madagascar extending to 11.6°S. Maximum transport is at 11.2°S with peak values greater than 3.60 Sv. Contour interval is .2 Sv. b) Total transport vs. time. The curve has been
is .2 Sv. b) Total transport vs. time. The curve has been

smoothed using a single pass of a 1-2-1 Hanning filter. Mean transport is 16.2 Sv. Oscillations occur from mid-March to mid-October with a period of 40 - 50 days. Peaks correspond to contours of maximum transport in (a)..... 56

Fig. 27: Eastern boundary throughflow: zonal transport at 115°E. a) Latitude-time contours of transport between Indonesia (9°S) and Australia (20°S) near the model eastern boundary. Solid (dashed) contours indicate eastward (westward) flow. Transport axes of the SEC and SECC are near 17°S and 22°S, respectively. Transport is in Sverdrups ($10^6 \text{ m}^3 \text{ s}^{-1}$) with a contour interval of .1 Sv. b) Annual cycle of throughflow. Mean transport is .4 Sv eastward with net westward (negative) transport only in February and July through September. Smoothed curve (single pass of a 1-2-1 Hanning) shows 36-day period oscillations. We note that periods of net eastward transport correlate well visually with maxima in the westward SEC as seen in (a)..... 62

Fig. 28: Meridional transport in the East African Coastal Current at 8.2°S, 40° - 43°E. a) Longitude-time contours. The blank region near 40°E is the African coast. Solid (dashed) contours show northward (southward) transport. Strong eddy activity seen four times during the year from 41°E to 43°E (dashed) contours show northward (southward) transport. Strong eddy activity seen four times during the year from 41°E to 43°E

with three additional eddies suggested. Grid noise is evident along the coast. Transport is in Sverdrups ($10^6 \text{ m}^3\text{s}^{-1}$) with a contour interval of .3 Sv. b) Total northward transport. Mean transport is 16.3 Sv. Maxima in May/June and in November hint at a seasonal cycle in phase with the onset of the SW and NE monsoons, respectively. The minimum in January is almost matched by those which immediately precede the maxima. Peaks show an oscillation with a period of about 50 days..... 66

Fig. 29: Time-longitude contours of meridional transport along the equator between the African coast and Gan ($43^\circ - 73^\circ\text{E}$). Solid (dashed) contours show northward (southward) transport. Offshore there is evidence of mixed Rossby-gravity waves with westward phase propagation and eastward group velocity. They are generated near the coast four to five times during the year. Transport is in Sverdrups ($10^6 \text{ m}^3\text{s}^{-1}$) with a contour interval of .4 Sv..... 69

List of Abbreviations

CW	clockwise (Southern Hemisphere cyclonic)
CCW	counterclockwise (anticyclonic)
EACC	East African Coastal Current
EKE	eddy kinetic energy
ENSO	El Niño - Southern Oscillation
EMC	East Madagascar Current
NMC	Northeast Madagascar Current
SEC	South Equatorial Current
SECC	South Equatorial Counter Current
SMR	Seychelles-Mauritius Ridge
SST	sea surface temperature
ULT	upper layer thickness

I. INTRODUCTION

Earth is a water planet, almost three quarters covered by oceans. The Southern Hemisphere oceans are more expansive than those of the Northern Hemisphere and have been less studied. Large areas of the Southern Hemisphere oceans are relatively, if not totally, unexplored, resulting in a scarcity of both oceanographic and meteorological data. The Indian Ocean is a predominately Southern Hemisphere ocean and data coverage is correspondingly thin. The efforts of the International Indian Ocean Expedition in 1962-1965 increased the oceanographic data available by a factor of five but emphasized the equatorial zone over southern regions (Wyrcki, 1971). Surface wind observations have traditionally been concentrated along commercial shipping lanes (Fig. 1). Globally, more than four times as many observations have been made during the last century in the Northern Hemisphere as compared to the Southern Hemisphere (Hellerman and Rosenstein, 1983).

The Indian Ocean is a particularly interesting ocean due most obviously to the seasonal monsoon reversals in winds and currents along the Somali Coast. Extensive observational effort has been focused on this northwest region, with relatively little attention paid to the southern subtropical circulation. A foundation is therefore lacking for understanding the effects of the Southern Hemisphere on the Somali Current and the equatorial regimes. Aside therefore lacking for understanding the effects of the Southern Hemisphere on the Somali Current and the equatorial regimes. Aside

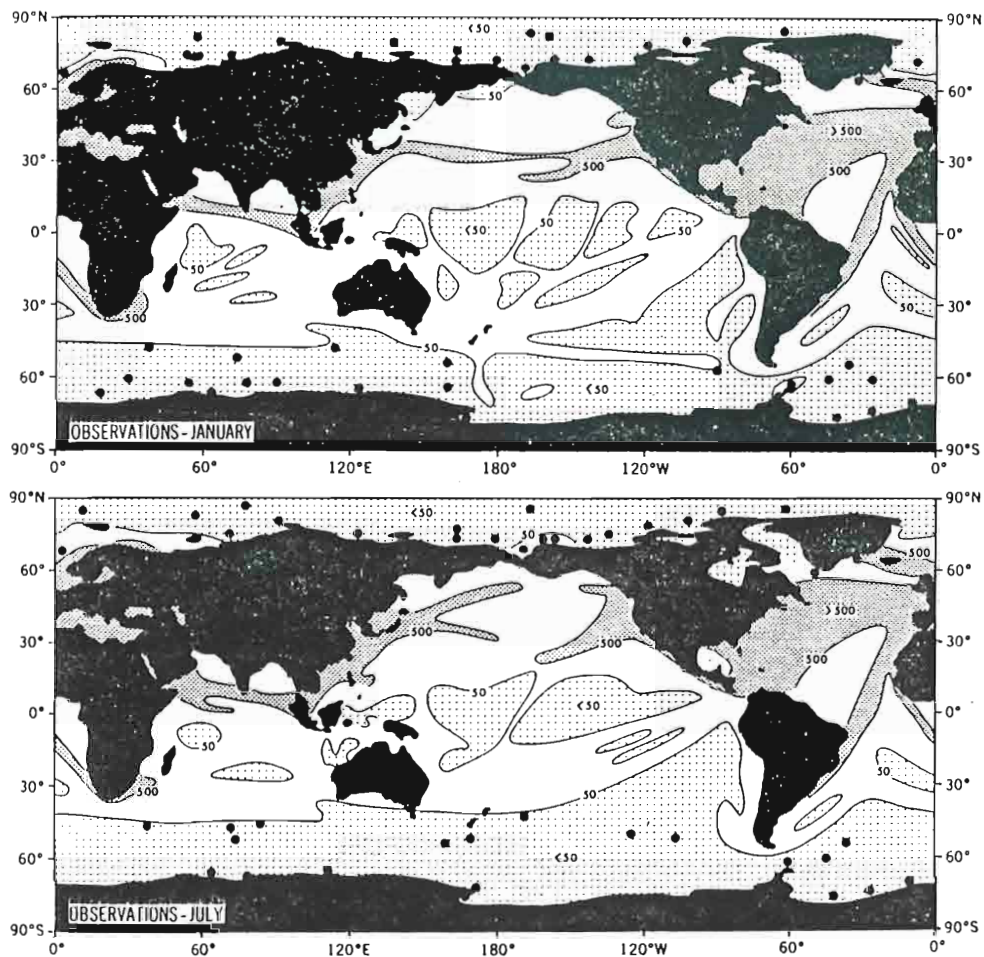


Fig. 1: Number of observations, N , from 1870 to 1976 per 2° latitude \times 2° longitude box, smoothed; light shading for $N < 50$, no shading for $50 < N < 500$ and dark shading for $N > 500$. From Hellerman and Rosenstein (1983).

from these intra-ocean interactions, knowledge of the southern Indian Ocean is necessary for understanding larger scale phenomena. Madden and Julian (1972) postulated an Indian Ocean source for observed 40-50 day atmospheric oscillations. Barnett (1983) investigated the interaction between Indian Ocean and Pacific Ocean winds and found strong coupling at interannual time scales and a strong connection to El Niño events in the Pacific. Nicholls (1984) found Indonesian sea surface temperature (SST) anomalies to lead Southern Oscillation and Pacific SST changes by about a season and suggested that interaction between ocean and atmosphere in the Indonesia-north Australia region may be a direct link between Indonesian SST and El Niño - Southern Oscillation (ENSO) events. ENSO events are often viewed as perturbations of the seasonal cycle. For reasons such as this, it is important to understand the seasonal cycle of the circulation.

Numerical models have proved useful in studying the response of the ocean to changing winds. They can help to integrate and interpret widely scattered observations. Modelling of the Indian Ocean at Florida State University has concentrated on the northwest (Somali Current) region of the Indian Ocean. Luther and O'Brien (1985) obtained good agreement with observations using a nonlinear reduced gravity model forced by a monthly mean climatology of ships' winds. Luther et al. (1985) forced the same model with FGGE level IIIb 1000 mb winds. A 23 year simulation of the circulation (Dube et al., 1988) used winds analyzed by Cadet and Diehl (1984). The 1000 mb winds. A 23 year simulation of the circulation (Dube et al., 1988) used winds analyzed by Cadet and Diehl (1984).

Bathythermograph and satellite data from the fall of 1985 verified a model simulation using actual wind observations (Simmons et al.,

1988). The dynamically active region around Socotra was especially well represented. A comprehensive review of modelling efforts in the tropical Indian Ocean can be found in Knox and Anderson (1985) and in Luther (1987).

We have recently extended the domain of the FSU model to cover the Indian Ocean to 25°S. In this paper we describe the model simulation of the seasonal circulation in the Southern Hemisphere and compare it with available observations and theory.

The dominant feature of the observed Southern Hemisphere circulation is the subtropical gyre with the westward flowing South Equatorial Current (SEC) as its northern boundary (Fig. 2; Pickard and Emery, 1982). The SEC splits at the coast of Madagascar into northward and southward branches. During the northeast monsoon (November to March), the northward branch rounds the tip of Madagascar and continues north along the African coast as the East African Coastal Current (EACC) to meet the southward Somali Current. They turn offshore together at about 3°S (Schott, 1983; Schott et al., 1988) and form the eastward South Equatorial Counter Current (SECC). During the southwest monsoon (May to September), the northward branch of the SEC feeds into the northward Somali Current and return flow is via the Southwest Monsoon Current.

The observational data from the southern Indian Ocean are concentrated in a few regions. Wyrski (1973) documented the existence of a zonal jet at the equator during monsoon transitions. concentrated in a few regions. Wyrski (1973) documented the existence of a zonal jet at the equator during monsoon transitions. The jet was accurately modelled by O'Brien and Hurlburt (1974) using a nonlinear, two layer, β -plane model. The time series at Gan (73°E)

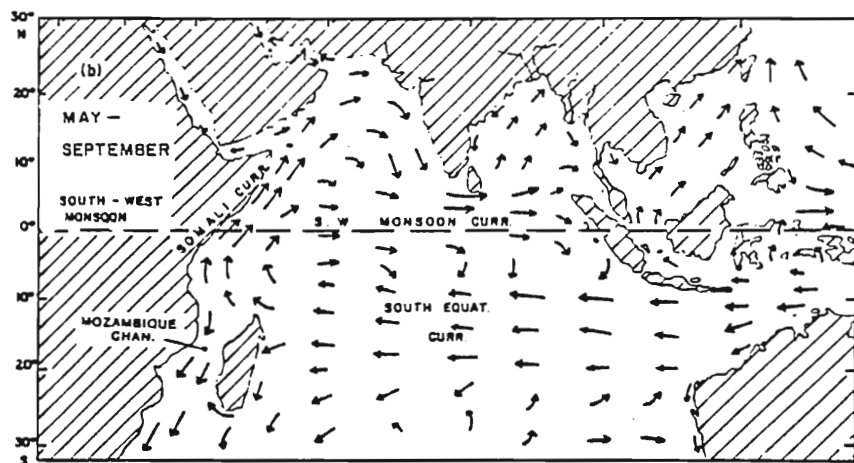
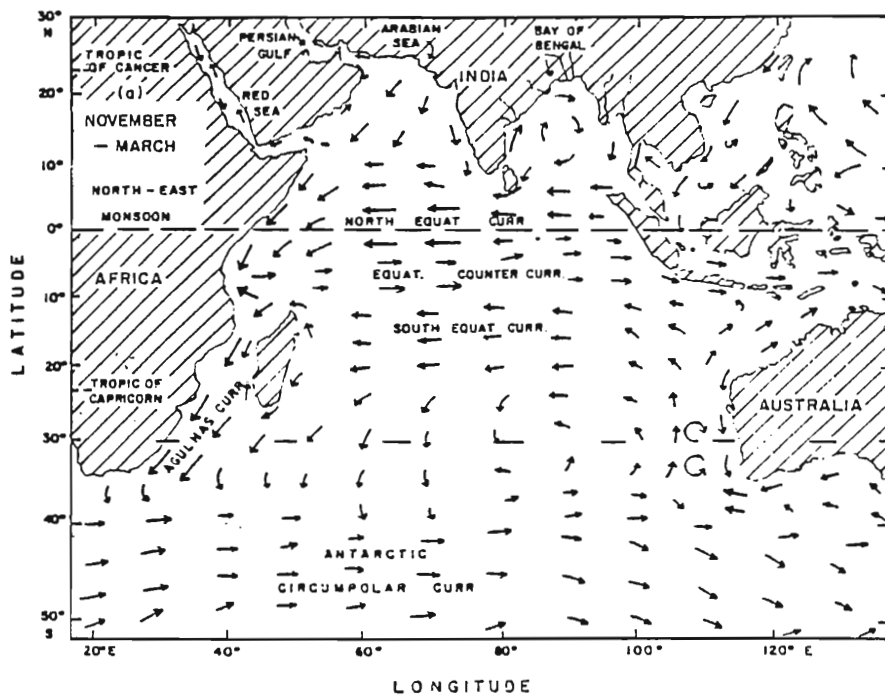


Fig. 2: Observed large scale surface circulation during NE and SW monsoons. From Pickard and Emery (1982).

presented by Knox (1976) clearly shows the reversals in equatorial currents. In the western equatorial Indian Ocean (49° - 62° W), zonal currents are also dominated by a semi-annual period (Luyten and Roemmich, 1982). Meridional velocities in that study, however, exhibited a prominent 26-day period, interpreted as evidence of mixed Rossby-gravity waves (Luyten and Roemmich, unpublished manuscript). South of the equator, several studies have found 40-50 day oscillations in the alongshore currents between 0° and 5° S (Mertz and Mysak, 1984) and off the northern tip of Madagascar (Quadfasel and Swallow, 1986; Schott et al., 1988). Schott et al., (1988) and Swallow et al. (1988) also present transport calculations for the boundary currents along eastern Madagascar and question the existence of a seasonal cycle. In addition to these observations, we compare our model results to the transports and oscillations in another reduced gravity model (Schott et al., 1988).

Observations in the Mozambique Channel have led to controversy in recent decades concerning flow along the African coast. Satre and da Silva (1984) presented a pattern of counterclockwise eddies as an alternative to the historical view of the continuous flow in the Mozambique Current. On the eastern side of the ocean, some effort has been focused on documenting and explaining the anomalous poleward flowing Leeuwin Current along the west coast of Australia (Thompson, 1984; McCreary et al., 1986). Additional studies at the eastern boundary have used various methods to estimate the throughflow from 1984; McCreary et al., 1986). Additional studies at the eastern boundary have used various methods to estimate the throughflow from the Pacific Ocean into the Indian Ocean through the Indonesian Islands (Godfrey and Golding, 1981; Fine, 1985). Gordon (1986) gives

an average throughflow of 9.2 Sv from all available estimates.

In the following pages, we first describe the model and the seasonal cycle in stress and curl fields of the winds used to force it. Next we present the results of the model simulation and highlight agreement with observations, looking first at the large scale circulation and then at the areas of interest noted above. We conclude with an overview of the wind driven circulation and a discussion of the strengths and weaknesses of the present model.

II. THE MODEL

The sharp density gradient observed with depth leads to modelling the ocean as a two layer system with an active upper layer over a deep motionless layer. The nonlinear reduced gravity equations describe the response of the upper layer to an applied wind stress. The equations are written in spherical coordinates due to the latitudinal extent of the model; longitude (ϕ) increases eastward and latitude (θ) increases northward. We define the eastward and northward components of the upper layer transport as $U=uH$ and $V=vH$, respectively, where (u,v) are the depth-independent (ϕ,θ) velocity components in the upper layer and H is the upper layer thickness (ULT). The equations of motion are therefore:

$$\begin{aligned} \frac{\partial U}{\partial t} + \frac{1}{a \cos \theta} \frac{\partial}{\partial \phi} \left(\frac{U^2}{H} \right) + \frac{1}{a} \frac{\partial}{\partial \theta} \left(\frac{UV}{H} \right) - (2\Omega \sin \theta) V \\ = \frac{-g'}{2a \cos \theta} \frac{\partial H^2}{\partial \phi} + \frac{\tau^{(\phi)}}{\rho_1} + AV^2U \end{aligned} \quad (1a)$$

$$\begin{aligned} \frac{\partial V}{\partial t} + \frac{1}{a \cos \theta} \frac{\partial}{\partial \phi} \left(\frac{UV}{H} \right) + \frac{1}{a} \frac{\partial}{\partial \theta} \left(\frac{V^2}{H} \right) + (2\Omega \sin \theta) U \\ = \frac{-g'}{2a} \frac{\partial H^2}{\partial \theta} + \frac{\tau^{(\theta)}}{\rho_1} + AV^2V \end{aligned} \quad (1b)$$

$$\frac{\partial H}{\partial t} + \frac{1}{a \cos \theta} \left[\frac{\partial U}{\partial \phi} + \frac{\partial}{\partial \theta} (V \cos \theta) \right] = 0 \quad (1c)$$

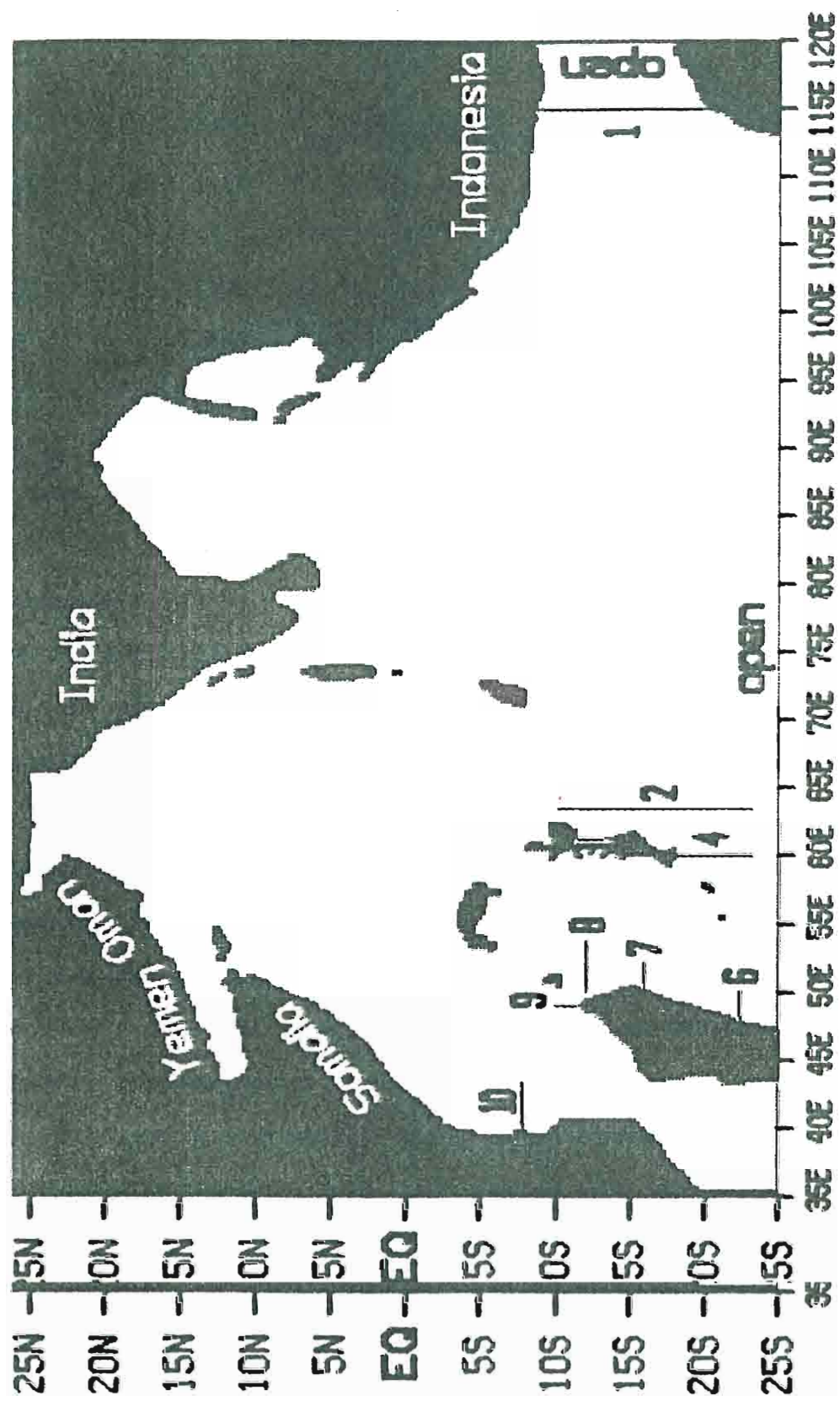
where $g' = \frac{(\rho_2 - \rho_1)}{\rho_2} g$ is the reduced gravitational acceleration, a is the radius of the earth, Ω is the earth's rotation rate, and A is a constant where $g' = \frac{(\rho_2 - \rho_1)}{\rho_2} g$ is the reduced gravitational acceleration, a is the radius of the earth, Ω is the earth's rotation rate, and A is a

kinematic eddy viscosity. The wind stress, $\vec{\tau} = [\tau^\phi, \tau^\theta]$ is applied as a body force over the upper layer (Luther et al., 1985).

For the model domain, realistic geometry of the Indian Ocean basin is used from 35°E to 120°E and from 25°S to 26°N as shown in Fig. 3. The boundary conditions at all solid (land) boundaries are the no-slip conditions: $u=v=0$. Most of the southern boundary along 25°S and a portion of the eastern boundary from 10°S to 20°S are open boundaries. The applied boundary condition is the Sommerfeld radiation condition described by Camerlengo and O'Brien (1980). The 200 m depth contour defines the model land boundaries. The shallow banks and islands in the domain include the Laccadive and Maldiva Islands, the Chagos Archipelago, and the banks around Socotra and along the Seychelles-Mauritius Ridge. These are all treated as land (closed) boundaries. Along the Seychelles-Mauritius Ridge, the major barriers to flow are the Seychelles (5°S, 55°E), Saya de Malha Bank (10°N, 63°E), and Nazareth Bank (15°N, 63°E). These banks are generally less than 30-40 m deep and are dotted with reefs and small islands. They are therefore likely to present significant barriers to the upper level flow in the region.

Equations (1) are solved numerically on a staggered grid as shown in Fig. 4. There is 0.1° between grid points in both zonal and meridional directions ($\Delta\phi, \Delta\theta$). The advective terms are computed by first averaging adjacent U and V and H values to form the desired product at the appropriate grid points and then using the standard, first averaging adjacent U and V and H values to form the desired product at the appropriate grid points and then using the standard, second-order accurate, centered finite difference approximation. The averaging helps to suppress grid scale noise. Energy is conserved

Fig. 3: Model geometry following the 200m depth contour. Land boundaries are shaded. This study focuses on the region south of 5°N. Islands in this region are identified in the text. Transect locations correspond to Table 1.



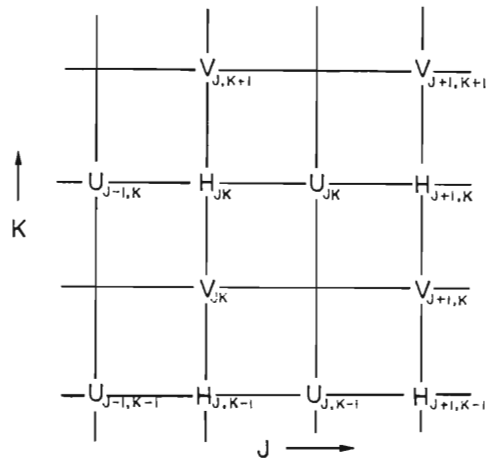


Fig. 4: Staggered grid used in finite difference approximation, showing relative location of U, V and H points. J is the index in the zonal (ϕ) direction and K is the meridional (θ) index.

but enstrophy is not. The equations are integrated in time using a leapfrog finite difference scheme, with a forward time difference used every 99th time step to eliminate the computational mode. The time step for the model integration is 20 minutes.

The model is forced by the mean monthly climatological winds of Hellerman and Rosenstein (1983). The Global Marine Sums wind speed climatology from the National Climate Data Center is used to compute and divide out an average drag coefficient from the Hellerman-Rosenstein stress data, recovering values of pseudo-stress, $\vec{W}|\vec{W}|$, where \vec{W} is the wind vector. This is done for reasons of consistency with other wind data products. The 2° by 2° gridded data set is interpolated to the model grid (0.2° between like grid points) using a bicubic spline interpolating procedure. τ^ϕ is applied at u grid points, τ^θ at v. We assume that each monthly mean represents the value at the middle of the respective month and interpolate linearly

between them to obtain a pseudo-stress data set covering a full annual cycle at the model time step of 20 minutes. We convert the pseudo-stress fields back to wind stress using the bulk aerodynamic formula:

$$\tau = \rho_a C_D \vec{W} |\vec{W}|$$

where ρ_a is the density of air and C_D is a constant drag coefficient. The drag coefficient thus becomes a parameter of the model rather than of the wind analysis. For the results presented here, $\rho_a = 1.2 \text{ kg m}^{-3}$ and $C_D = 1.5 \times 10^{-3}$.

The model is integrated from rest starting at 0h GMT on 16 December with an initial ULT set at $H_0=200\text{m}$. For the results presented here, we set the kinematic eddy viscosity $A=750 \text{ m}^2\text{s}^{-1}$ and the reduced gravity $g'=0.03 \text{ ms}^{-2}$. An exponential taper with an e-folding time of 20 days is applied at the start of the first year of integration to reduce the initial transients. For simplicity, the model year has 360 days, with 30 days in each month. The time for a baroclinic Rossby wave to cross the basin at 25°S is on the order of a decade. The model is spun up for 12 years, and the final year is interpreted here.

III. THE WINDS

The seasonal cycle of winds over the Indian Ocean is dominated by the monsoon reversals in the Northern Hemisphere. Differential heating drives oscillations in Northern and Southern Hemisphere pressure systems causing seasonal changes in the winds. During the Northern Hemisphere winter, a high pressure center exists over central Asia, driving northeasterlies across the northern Indian Ocean into a trough near the equator (NE monsoon). During the Southern Hemisphere winter, a high pressure center develops over Madagascar with concurrent intensification of the southeast tradewinds. The trades blow across the equator, are diverted northeastward by the African highlands, and blow into a trough situated over northern India (SW monsoon). We describe this annual cycle in the climatological winds used to force the model (Hellerman and Rosenstein, 1983). We look first at the cycle of reversals along the African coast, then at the equatorial region and lastly at the southeasterly tradewinds. Figs. 5 through 12 show the cycle of winds and curl fields over the entire model domain.

The northeast (NE) monsoon lasts from November through March with strongest northeasterly (southwestward) winds in January along the Somali coast to about 15°S (Fig. 5). The northeasterly winds are associated with negative curl along the coast and positive curl on the eastern side of the jet axis (Fig. 6). Negative curl in the associated with negative curl along the coast and positive curl on the eastern side of the jet axis (Fig. 6). Negative curl in the

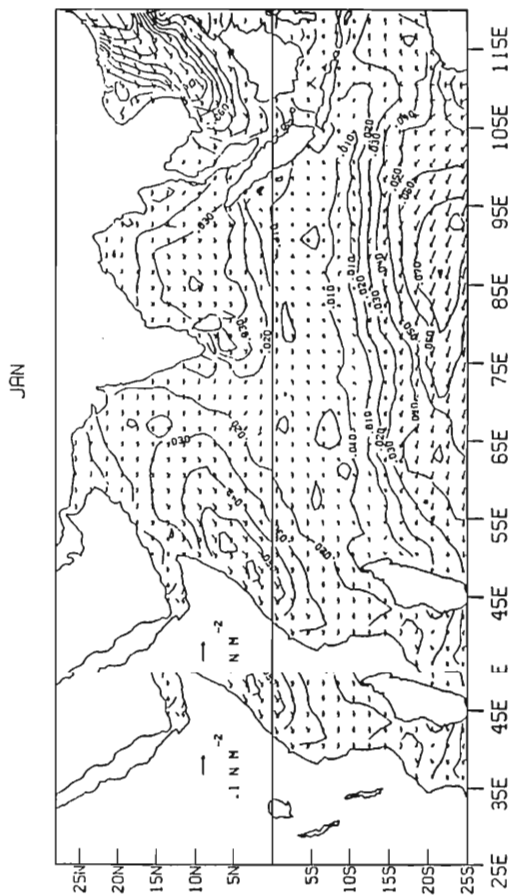
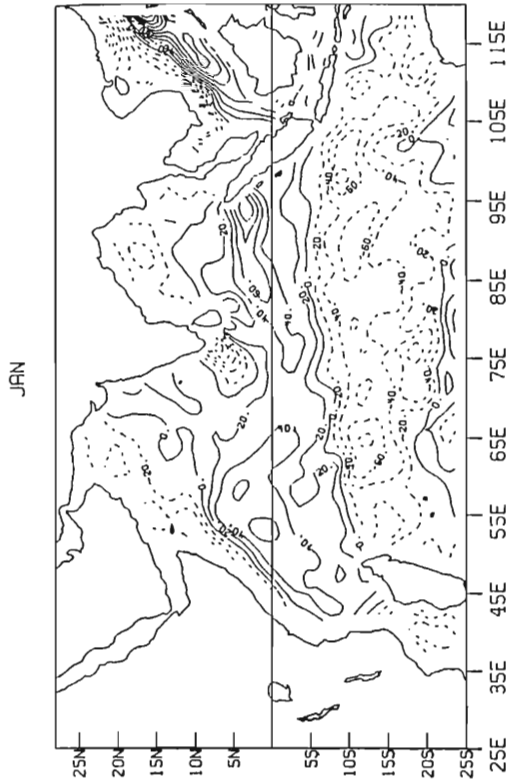


Fig. 5: Wind stress for January 16 during the NE monsoon. Vectors are wind stress direction and magnitude (see scale on Somali peninsula). Contour interval is 0.1 N m^{-2} . Winds over the South China Sea are not used by the model. Strongest winds are found in the southeast trades between 20°S and 25°S , 85°E to 95°E . Monsoon winds are maximum on either side of 5°N near the African coast. Northeasterly winds are also found east of India. Winds at the eastern boundary are westerly.

Fig. 6: Wind stress curl for January 16 during the NE monsoon. Contour interval is $2 \times 10^{-8} \text{ Nm}^{-3}$. Labels are in units of 10^{-9} Nm^{-3} . Curl fields have been smoothed both zonally and meridionally with a single 1-2-1 Hanning filter. A band of strong negative curl extends across the basin between $5^\circ\text{--}10^\circ\text{S}$ and 20°S . There is negative curl along western Australia, in the Mozambique Channel and along the Somali Coast. Strong positive curl is found in the region of the southern subtropical gyre. A band of strong positive curl between 10°N and 5°S extends south along the African coast into the northern Mozambique Channel.

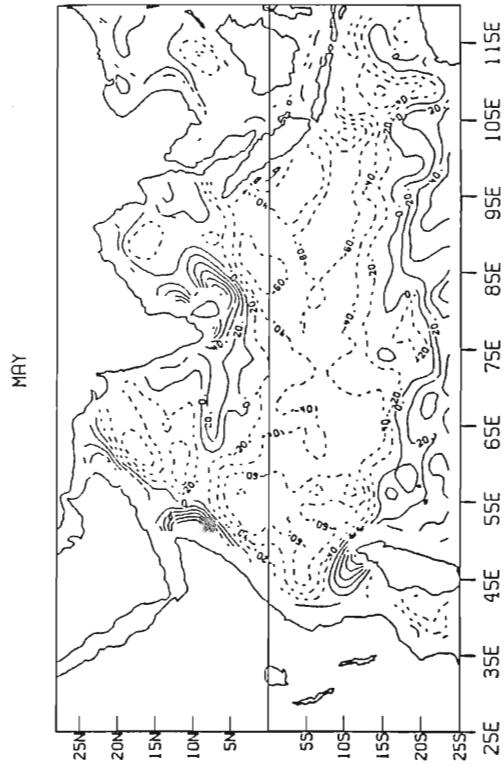


Fig. 8: Wind stress curl as in Fig. 6 for May 16 at the beginning of the SW monsoon. Strong negative curl from 5°N to 15°S, in the northern Arabian Sea and Bay of Bengal, and in the Mozambique Channel. Strong positive curl south of 15°S, along the Somali and Omani coasts and around the tip of India.

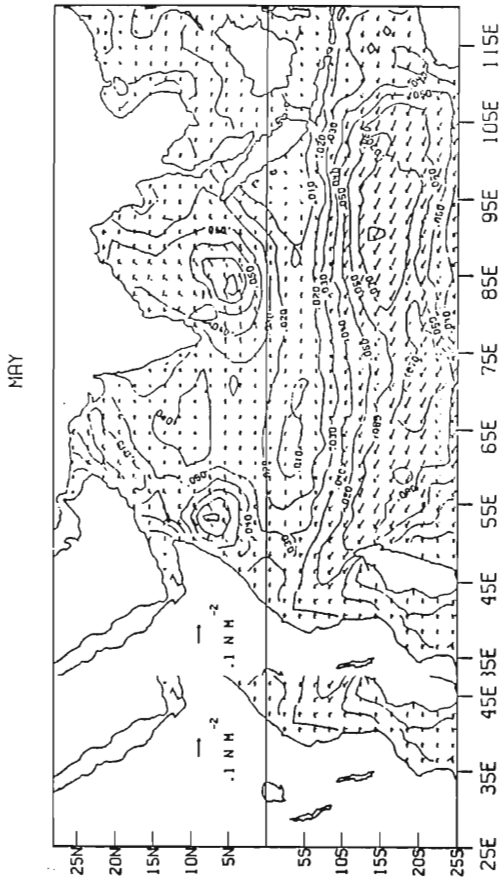


Fig. 7: Wind stress as in Fig. 5 for May 16 at the beginning of the SW monsoon. Strongest winds are still in the southeasterly trades. The tradewindwesterly extend across the equator with southwesterlywesterly flow along the Somali Coast. Strong windsg westerly in the Bay of Bengal are also southwesterlywesterly. Westerly winds are seen at the equator with easterly winds at the eastern boundary.

JUL

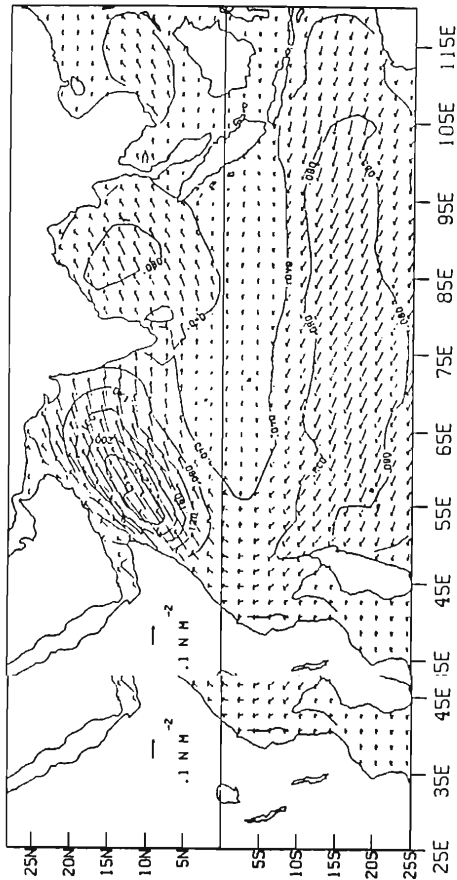


Fig. 9: Wind stress as in Fig. 5 for July 16 at the height of the SW monsoon. Contour interval is $.04 \text{ Nm}^{-2}$. Maximum southwesterlies are found over the Arabian Sea with weaker southwesterlies in the Bay of Bengal. The southeast trades are nearing peak strength and coverage (August). Easterly westerly winds at the western boundary.

JUL

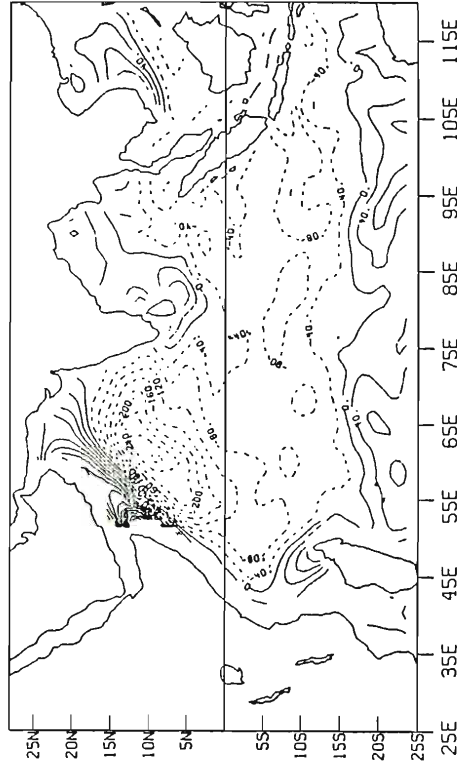


Fig. 10: Wind stress curl as in Fig. 6 for July 16 at the height of the SE monsoon. Contour interval is $4 \times 10^{-8} \text{ Nm}^{-3}$. The overall pattern seen in May has intensified with sharp gradients between regions of strongly positive and negative curl. Positive curl in the south extends around the tip of Madagascar and northward along the African coast. Negative curl covers the interior of the domain.

0CT

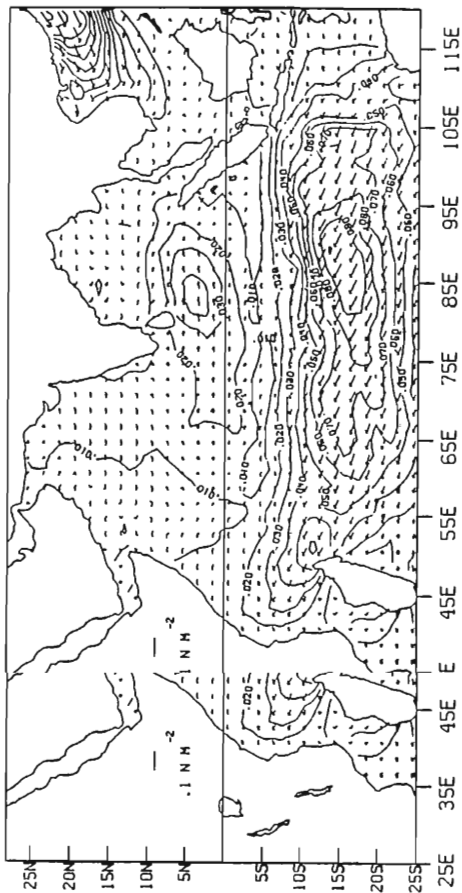


Fig. 11: Wind: Wind stress as in Fig. 5 for October 16 during the SW to NE monsoon transition. Southeast trade winds are still strong, extending to the African coast. Northern hemisphere winds are weak with northerly winds appearing in the northern Arabian Sea. A jet of westerly winds is centered at 5°N , 85°E . Weak winds at the eastern boundary changing to westerly.

0CT

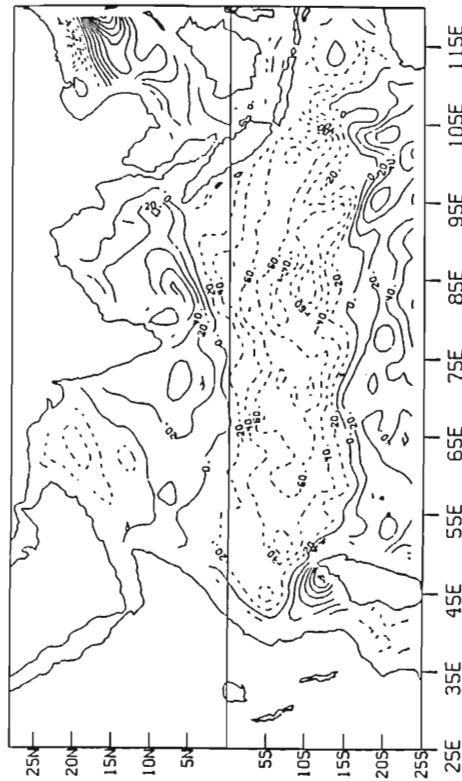


Fig. 12: Wind stress curl as in Fig. 6 for October 16 during the SW to NE monsoon transition. Strong positive curl across the south to 15°S with strong negative curl to the equator. The biggest changes since July are found in the northwest where there is a mixture of weak positive and negative curl with stronger negative curl appearing in the far north. Curl at the African coast is still positive. The region of positive curl around India has spread and weakened since July.

Mozambique Channel south of 15°S is due to the convergence of the northerly winds with the Southern Hemisphere tradewinds. Patterns of stress and curl remain similar in February through March although the strength of both decreases as the NE monsoon decays. Winds around Madagascar become southerly. By April the winds north of Madagascar are southeasterly as the trades extend to the African coast. Stress and curl fields north of the equator are weak.

The onset of the SW monsoon is evident in May (Fig. 7) in the southerly flow curving along the entire African coast. Curl patterns have changed sign north of 10°S (Fig. 8). These stress and curl patterns intensify dramatically during May through July (Figs. 9, 10). The sharp curl gradient in the Arabian Sea follows the axis of the southwesterly Findlater jet (Findlater, 1971). The SW monsoon decays in August and September with the transition from SW to NE monsoon occurring in October (Figs. 11, 12). Weak winds in the northern Arabian Sea have reversed, becoming northerly. There are still weak southerly winds extending across the equator, creating a westerly convergence in the Arabian Sea. The NW monsoon intensifies through the end of the year with reversals in direction of the wind stress and sign of the curl patterns along the African coast.

Westerly winds predominate in the equatorial region away from the coast. During both monsoons, equatorial winds are relatively weak but relatively strong westerly maxima are present during transition months of April and October. During the height of the NE monsoon, equatorial winds have a northerly component backing to westerly south of the equator (Fig. 5). Curl is positive from 5°N to

5°S (Fig. 6). Winds are westerly east of about 70°E in March extending to 55°E in April when a westerly maximum is located near 2°N, 82°E. In April, there is near zero wind stress curl all along the equator and extending into the Southern Hemisphere between about 55°E and 70°E. By May, winds have strengthened and acquired a southerly component from 75° to 90°E (Fig. 7). Wind stress curl at the equator has become strongly negative in the east and west with a gradient to positive curl around the tip of India (Fig. 8). As in the coastal regions, these patterns intensify through July (Fig. 9, 10) and decay through September. During the October transition from SW to NE monsoon, the changing winds in the Arabian Sea converge near the southern tip of India forming a westerly maximum at 5°N, 80° - 85°E. Winds are westerly at the equator between 65°E and 95°E (Fig. 11). Near zero wind stress curl is again found along the equator (Fig. 12). Equatorial winds weaken and become northerly by December with some westerlies still seen east of about 80°E.

The tradewinds in the Southern Hemisphere are southeasterly throughout the year. In January they are strongest in the southeast, turning easterly at about 60°E, and converging over Madagascar with the NE monsoon winds crossing the equator (Fig. 5). Southerly winds at the coast of Australia diverge to contribute both to the SE trades and to westerly winds at the eastern boundary of the model. Near zero wind stress curl is found across the basin near 20°S, with negative curl to the north and positive to the south (Fig. 6). zero wind stress curl is found across the basin near 20°S, with negative curl to the north and positive to the south (Fig. 6).

The trades strengthen in April, reaching the African Coast, and in May they extend across the equator with the onset of the SW

monsoon (Fig. 7). This cross-equatorial extension of the SE trades is evident in the first eigenvector map shown by Breidenbach (1988) from an analysis of wind stress over the Indian Ocean from 1977 to 1985. This pattern accounts for 65.5% of the variance of the data set. The third eigenvector (3.2%) shows most of the interannual variability to be in the trades south of about 12°S. This variability, of course, is absent in the climatological winds.

At the eastern boundary, winds become easterly with the strengthening of the trades in May. The zonal bands of positive and negative curl broaden and move northward. The line of zero wind stress curl is now near 17°S (Fig. 8). It moves to 15°S as the trades peak in July and August (Fig. 9, 10) and remains there through November as the trades weaken and maximum winds retreat to the east (Fig. 11, 12). Winds at the eastern boundary become westerly in November.

IV. RESULTS

1. Large scale circulation

The major flow patterns of the Indian Ocean are well represented by the model. The South Equatorial Current (SEC), the South Equatorial Counter Current (SECC), the Somali Current, and equatorial jets are all easily identified. Figs. 13, 15, 18, and 19 show the major features of the circulation and characteristics of the seasonal cycle in quadrants of the domain. In the following discussion, we describe the westward flow in the SEC, the active western boundary region, the equatorial jets, and the eastward return flow in the SECC. These are summarized in Fig. 20. We also note the similarity of model ULT patterns to maps of dynamic height and to thermocline climatologies.

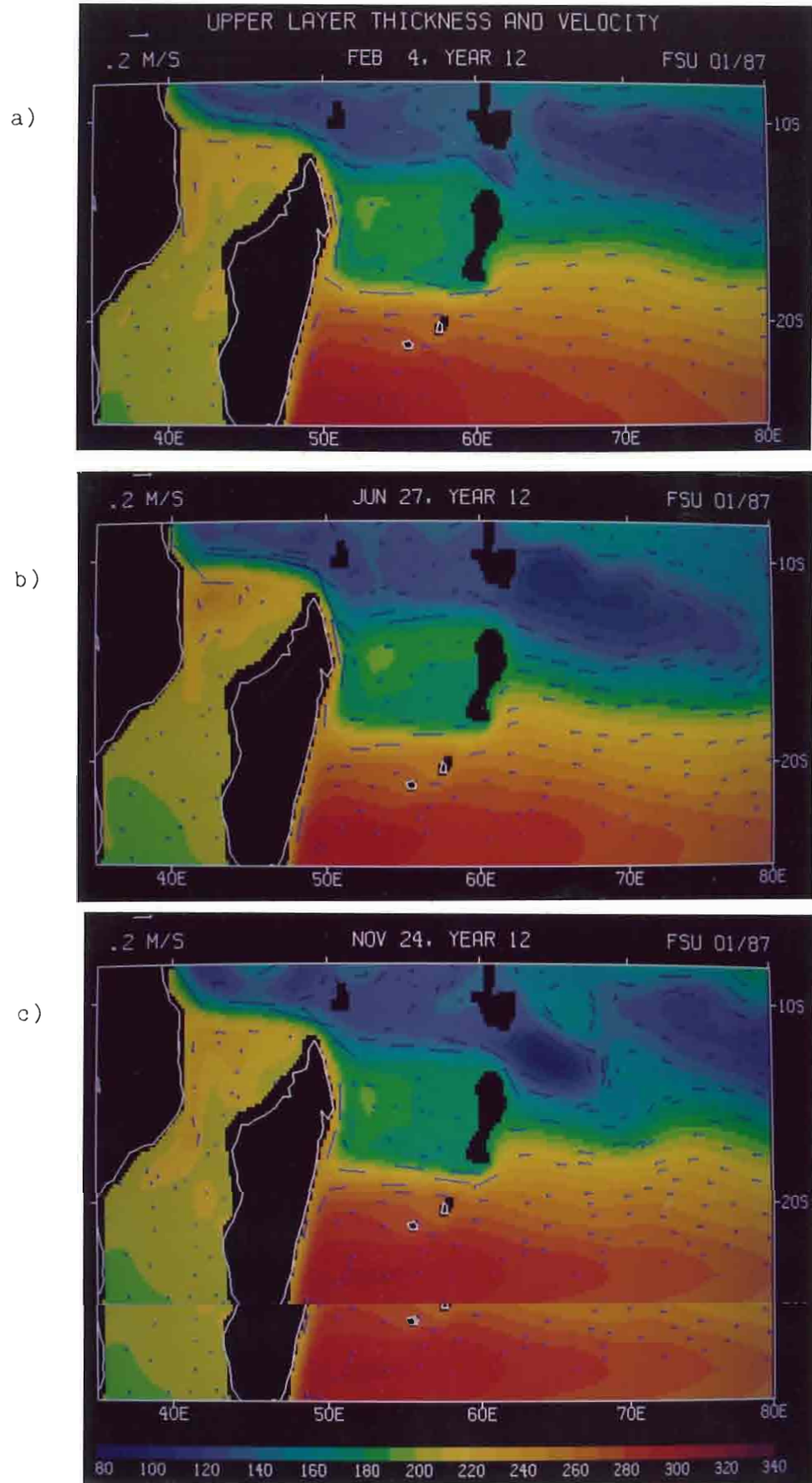
The SEC is observed between 8°S and 15°-20°S (Godfrey and Golding, 1981; Pickard and Emery, 1982; Gordon, 1986). The model SEC flows westward at 12°-22°S in the northern regions of the subtropical gyre (Figs. 13, 19). Maximum transport is found at about 17°S across the ocean basin (see Figs. 21a, 27a). The line of zero wind stress curl in the wind forcing is generally found between 15°S and 20°S. This is the limit of the wind-driven subtropical gyre as there is no meridional transport across it according to the Sverdrup (1947) balance: $\beta V \propto \hat{k} \cdot \text{curl } \vec{\tau}$, where V is meridional transport, $\vec{\tau}$ is the wind stress, \hat{k} is the vertical component, and β is the change of the balance: $\beta V \propto \hat{k} \cdot \text{curl } \vec{\tau}$, where V is meridional transport, $\vec{\tau}$ is the wind stress, \hat{k} is the vertical component, and β is the change of the

Fig. 13: Model velocity vectors and upper layer thickness (ULT) contours in the SW quadrant of the domain. Velocity scale vector in the upper left. Contour scale along the bottom. The large island 45° - 50° E is Madagascar with the Farquhar group of islands to the northeast. Saya de Malha and Nazareth Banks are at 60° E.

a) February 4. Annual Rossby wave near 10° S, 70° E in SEC-SECC shear zone is beginning to "feel" the blocking of the Seychelles-Mauritius Ridge. The wave from the previous year has contracted to a small eddy passing between the banks at 60° E. Subtropical gyre is seen at the southern boundary. Anticyclonic circulation in the northern Mozambique Channel.

b) June 27. Rossby wave contracting, moving south east of the Seychelles-Mauritius Ridge. Strong high pressure cell in the northern Mozambique Channel.

c) November 24. Oscillations in SEC due to Rossby wave propagation and blocking at 60° E. Recirculation due to eddy activity west of the Farquhar Islands. Trough in Mozambique Channel extends almost to 20° S.



Coriolis parameter with latitude. Godfrey and Golding (1981) calculated a zonal jet in the mass transport function between 10°S and 15°S. They noted also that throughflow from the Pacific continues zonally across the basin and suggested that this is possibly linked to the westward propagation of internal Rossby waves.

North of the SEC, in the clockwise shear zone between the SEC and the SECC, the model shows a region of westward propagating Rossby waves (Figs. 13, 19). A wave is generated annually at the eastern boundary by the cycle of local winds. Westerly winds are found at the eastern boundary between November and February. East of 110°E the accompanying curl is positive along Indonesia and negative along Australia. Winds are easterly and curl is reversed during April through September. The Rossby wave excited by these annual wind reversals propagates unhindered across the basin until it begins to "feel" the Seychelles-Mauritius Ridge (SMR) at 60°E (Figs. 13a, 14a).

The banks along the SMR partially reflect the incoming Rossby wave and an eddy is formed to the east of the banks due to nonlinear effects in the reflected wave packet (cf. Pedlosky, 1987, sec. 3.23). As the eddy develops, it moves slightly southward. Passage of the eddy through the break in the ridge generates meridional oscillations in the current across to Madagascar. The phase speed of the oscillations is calculated to be 9.3 cm s^{-1} and the period is about 70 days. Nazareth Bank blocks the SEC at 60°E and the current ~~the~~ oscillations is calculated to be 9.3 cm s^{-1} and the period is about 70 days. Nazareth Bank blocks the SEC at 60°E and the current splits to flow around the northern and southern ends and continue westward. The southern branch impinges on the coast of Madagascar

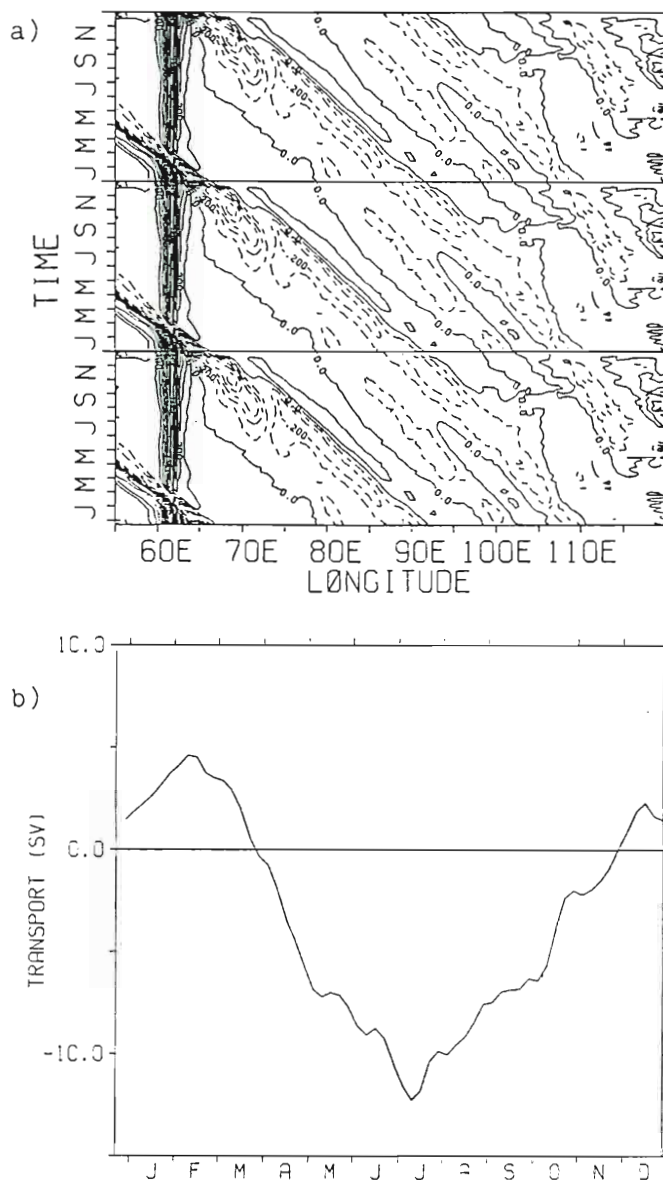


Fig. 14: Meridional transport at 13°S. Transect cuts through the Rossby wave zone from 55° to 120°E. a) Longitude-time contours. One year of data is repeated three times to show the propagation of the Rossby wave. Solid (dashed) contours indicate northward (southward) flow. A single Rossby wave is generated each year near 110°E which has a westward phase speed of 9.3 cm s^{-1} as measured from the center of the figure. Transport is in Sverdrups ($10^6 \text{ m}^3 \text{ s}^{-1}$) with a contour interval of .1 Sv. b) Annual cycle. Net transport at this latitude is northward (positive) December through March and southward (negative) April through November. The strong annual signal indicates an annual Rossby wave. There are hints of oscillations with a period of about 36 days. The curve has been smoothed with a single pass of a 1-2-1 Hanning filter.

with maximum transport at 18.7°S (see Fig. 22) and splits into the southward flowing East Madagascar Current (EMC) and an unnamed northward branch, which we will call the Northeast Madagascar Current (NMC).

The NMC combines at the northern tip of Madagascar with the westward flow between Saya de Malha and Nazareth Banks. This current rounds the northern tip of Madagascar (Cape Amber) and continues westward to the African coast. A small portion of this flow enters the Mozambique Channel to the south and circulates as an counterclockwise high pressure cell between Madagascar and the African coast. This circulation will be addressed later.

Most of the flow reaching the coast of Africa turns northward as a strong tradewind-driven boundary current, the East African Coastal Current (EACC). During the NE monsoon this current flows in conflict with the alongshore pressure gradient set up by the monsoon winds through differential Ekman pumping. Anderson and Moore (1979) proposed a mechanism of inertial overshoot whereby the relaxation of the NE winds would allow the EACC to push further northward, causing an early reversal of the Somali Current. Fig. 15a shows the EACC being met by the southward flowing Somali Current early in the year (NE monsoon) and turning offshore at $2^{\circ}\text{--}3^{\circ}\text{S}$ in agreement with observations (Schott et al., 1988). Westward equatorial currents augment the Somali Current at this time. The convergence between the EACC and the Somali Current moves to about 4°S in February/March with augment the Somali Current at this time. The convergence between the EACC and the Somali Current moves to about 4°S in February/March with a clockwise (CW, cyclonic) eddy to the south and an counterclockwise (CCW, anticyclonic) eddy to the north. Although the northeasterlies

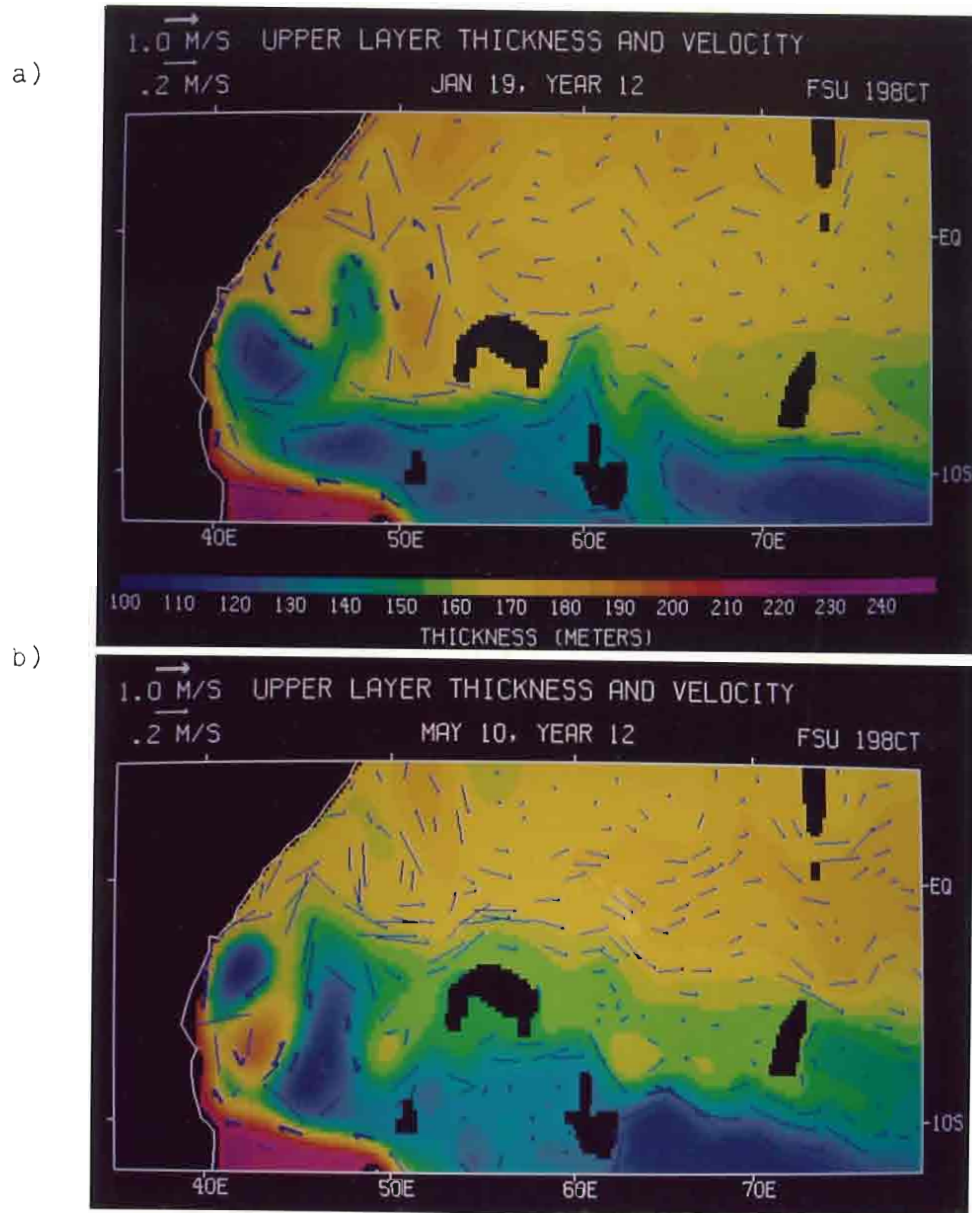
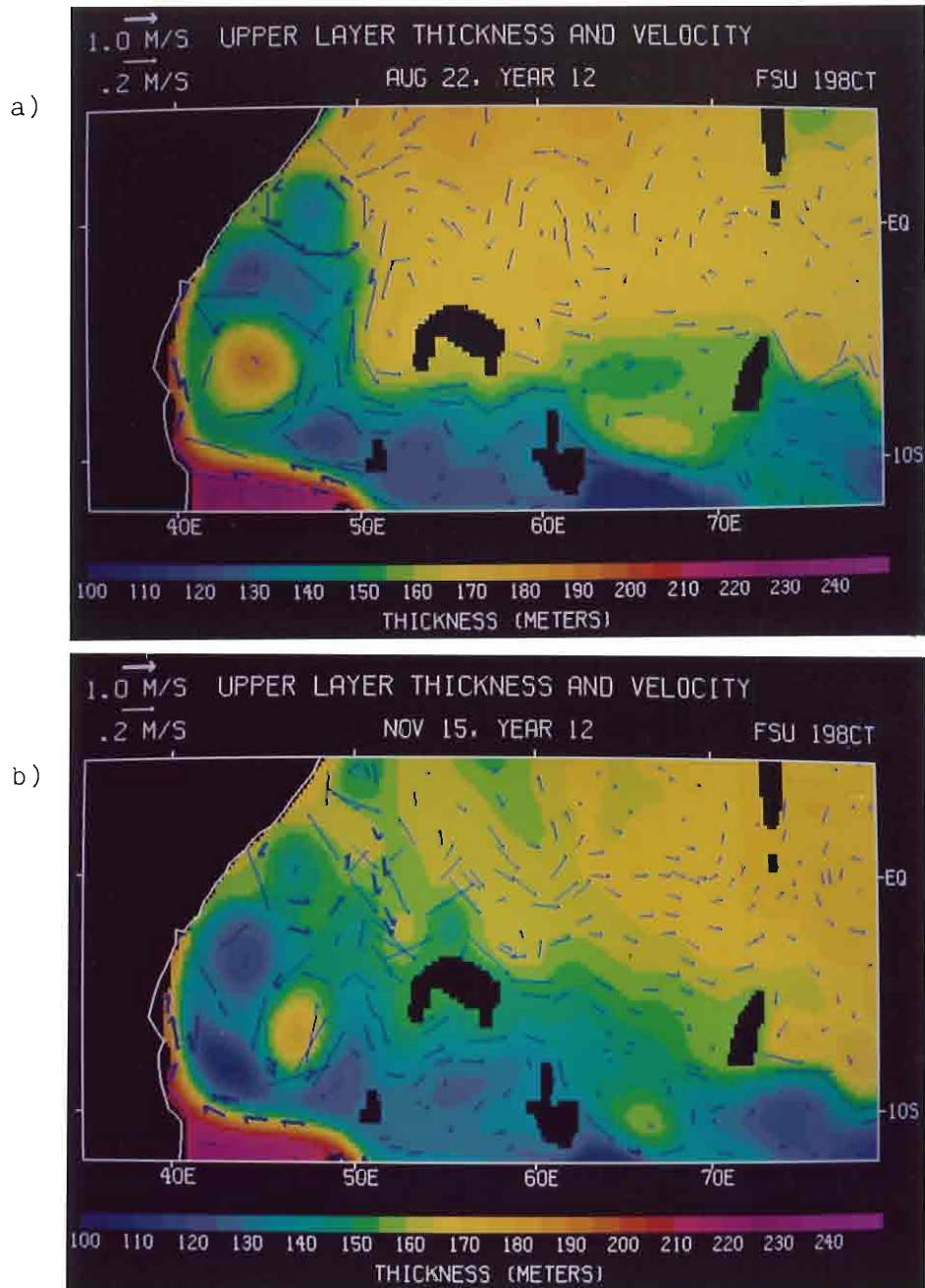


Fig. 15: As in Fig. 13 for the NW quadrant for the domain. Note the two velocity scales. Cape Amber at the tip of Madagascar is just visible at 49°E. Other "land" regions are the Farquhar Islands NE of Cape Amber; the Seychelles at 15°S, 55°E; Saya de Malha Bank at 61°E; the Chagos Archipelago at 7°S, 72°E; and the Maldives and Gan along 73°E.

a) January 19. EACC and Somali Current meet and turn offshore near 3°S. Flow meanders eastward through the islands to feed the SECC with strongest flow between 6°S and 10°S. Equatorial currents are westward. Equatorial Rossby waves visible at 4°N and 4°S near 50°E.

a) January 19. EACC and Somali Current meet and turn offshore near 3°S. Flow meanders eastward through the islands to feed the SECC with strongest flow between 6°S and 10°S. Equatorial currents are westward. Equatorial Rossby waves visible at 4°N and 4°S near 50°E.

b) May 10. Eddy activity between the equator and 10°S is discussed in the text. Outflow from the region now includes strong eastward flow at the equator. Eastward transport is increasing ULT in the east.



c) August 22. The "southern gyre" just south of the equator has spun off a clockwise eddy into the northern hemisphere. Meridional velocities are prominent at the equator during this transition to eastward flow.

spun off a clockwise eddy into the northern hemisphere. Meridional velocities are prominent at the equator during this transition to eastward flow.

d) November 15. Eddies bracketing the equator are moving south under the influence of the NE monsoon. Outflow from their convergence zone evidences strong cross equatorial oscillations. Equatorial currents are beginning to reverse in the east.

are relaxing, this strong CCW circulation remains through most of March before weakening and slowly giving way to northward flow at the coast. We see a delayed adjustment of the pressure gradient and inertial forces just mentioned. The curl pattern continues to contribute to maintenance of the alongshore pressure gradient through March which opposes the tendency toward inertial overshoot. The winds veer easterly in March south of the equator. They are southerly by April and then enhance the inertial flow of the EACC.

By mid-April, the transition from NE to SW monsoon is seen in the reversal to eastward flow at the equator (Fig. 15b) with strong northward flow all along the African coast by June persisting through July and August. During the remainder of the year, the coastal flow to the north of the equator is relatively weak and chaotic, with mixed patches of northward and southward flow. Equatorial Rossby waves may contribute to pockets of northward flow as their clockwise circulations impinge on the coast.

Observations have focused on the eddies north of the equator in the Somali Current region. Fig. 15 shows the eddy activity and recirculation in the model solutions south of the equator in the region of the EACC. Similar solutions have been obtained by Kindle (Schott et al., 1988) from a similar reduced-gravity model. Fig. 16 shows the eddy kinetic energy (EKE) for the year in the region between Madagascar and the equator. Maximum EKE in the region is found near 3°S , 45°E . High EKE is found in the EACC south to about between Madagascar and the equator. Maximum EKE in the region is found near 3°S , 45°E . High EKE is found in the EACC south to about 9°S . We will later discuss the oscillations in the EACC associated with this eddy activity. A zonal series of relative maxima in EKE is

located at about 1°S . The maxima are approximately 250 km apart and decay eastward. The meridional elongation of the maxima resembles the strong meridional velocities associated with the eddies and the oscillations in the region.

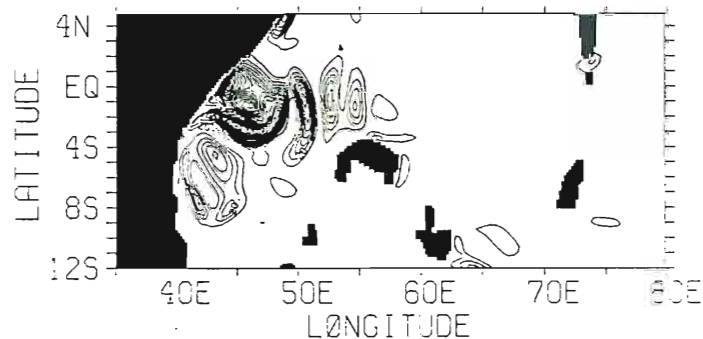


Fig. 16: Eddy kinetic energy (EKE) for one year in the equatorial region near the African coast, $40^{\circ} - 80^{\circ}\text{E}$, $5^{\circ}\text{N} - 12^{\circ}\text{S}$. EKE is concentrated at the coast south of the equator with a maximum of $280 \times 10^{-4} \text{ m}^2 \text{ s}^{-2}$ near 3°S . Zonal relative maxima are separated by approximately 250km. Labels are in units of $10^{-4} \text{ m}^2 \text{ s}^{-2}$ with a contour interval of $1.0 \times 10^{-3} \text{ m}^2 \text{ s}^{-2}$.

This region of eddy activity is continually evolving. This is the source region for the Somali Current during the SW monsoon. In the model it is seen as an extension of the tropical gyre formed by the SEC and SECC. The strong shears in the region result in eddies being pinched off of this gyre extension. They circulate in a clockwise fashion in this approximately 10° by 10° region, merging and reinforcing each other. Counterclockwise (CCW) eddies are also generated by the shear flows, appearing just west of the Seychelles near 5°S . Alternatively, these may be manifestations of equatorial Rossby waves generated by the shear flows, appearing just west of the Seychelles near 5°S . Alternatively, these may be manifestations of equatorial Rossby waves (O'Brien et al., 1981). They propagate westward to the African coast, cutting through the clockwise circulations, and are

absorbed into the EACC.

In late January and February, CCW flow is found to the north of the EACC-Somali Current convergence with CW flow to the south (Fig. 15a). As noted above, this split at the coast remains through March although the offshore flow begins to meander. A CW eddy pinches off near 48°E in early March and is pushed northward by an CCW eddy (Rossby wave) appearing later in the month. It weakens and is absorbed into other eddies. The CCW eddy moves westward, pinching off a CW eddy against the coast and blocking another to the east (Fig. 15b). These three move in a clockwise fashion, the CCW eddy is absorbed into the EACC, and a second CCW eddy appears west of the Seychelles in late May. The CW eddies coalesce and elongate against the coast until this new CCW eddy splits them in June. New CCW eddies appear one to two months apart through the remainder of the year and move westward to join the EACC, keeping a CW eddy relatively isolated just south of the equator. This eddy oscillates on a clockwise path which edges across the equator. This is interpreted as the "southern gyre" of two large eddies observed along the Somali coast (Bruce, 1973; Swallow and Fieux, 1982; Swallow et al., 1983; Schott, 1983; Luther et al., 1985). The formation of the "southern gyre" may be caused by alongshore winds near the equator without requiring the forcing of the SE trades as shown by McCreary and Kundu (1988); however, the curl of the wind near the equator can be important in determining the latitude at which the current turns (1988); however, the curl of the wind near the equator can be important in determining the latitude at which the current turns offshore (Anderson and Moore, 1979). Inertial effects will certainly modify this result. Salinity observations show the water from the

EACC to recirculate south of the equator while the equatorial currents are fed by water from north of the "southern gyre" (Swallow et al., 1983). The CW "great whirl" forms between 4° and 6° N (Luther et al., 1985), while the "southern gyre" is observed south of 5° N, slightly north of our model eddy.

Observations show the southern eddy to move northward and coalesce with the "great whirl" in September (Bruce, 1973). McCreary and Kundu (1988) conclude from their model results that the migration of the southern gyre is due to the ocean not being in equilibrium with peak monsoon winds. The migration has been simulated without the SE trades (Luther et al., 1985) and was seen in 14 years of a 23 year simulation (Dube et al., 1988). In the other 7 years during which the "southern gyre" and "great whirl" were clearly present, a blocking flow developed which prevented the northward migration of the "southern gyre". In this model simulation, westward equatorial flow in early August interacts with the near-equatorial CW eddy and spins off an CCW eddy into the Northern Hemisphere (Fig. 15c). (Both eddies are cyclonic in their respective hemispheres.) This two eddy system causes convergence at the equator near the coast with the northern eddy blocking the northward movement of the "southern gyre". The climatological wind forcing used in this simulation therefore favors the blocking situation, which is the less frequent condition in the 23 year simulation. The alongshore winds were anomalously strong in those 7 years; however, that simulation does not include the effects of the Southern Hemisphere trade winds, which alter the flow characteristics in this region. In this model

simulation, the cross-equatorial eddy pair begins to move south with the transition to the NE monsoon in October/November and southward flow across the equator is reestablished (Fig. 15d). The "southern gyre" is a persistent feature in this region of the model although it is more prominent during the SW monsoon.

Strong cross-equatorial inertial oscillations occur as eddies interact with each other and with the monsoon reversals north of the equator. Fig. 15d shows especially strong oscillations in November. These contribute to the wave motions seen in equatorial currents which will be discussed later.

The equatorial currents reverse four times during the year in agreement with the equatorial jets documented by Wyrtki (1973). He noted the appearance of the jet during monsoon transitions in April and May and in September and October. Strongest flow was found between 60°E and 90°E . Fig. 17 clearly shows the two periods of eastward flow in the model. Duration and latitudinal extent of this eastward flow exceed observations somewhat but agreement with observations is generally good. Except in August, transitions propagate from east to west as reported from buoy trajectories by Reverdin et al. (1983) and from a current meter array at 49°E to 62°E by Luyten and Roemmich (1982). The following chronology refers to flow east of about 55°E , away from the eddy confusion near the coast. West of the Maldives and Gan (73.5°E), model geometry includes numerous islands which affect the flow; this area is more coast. west of the Maldives and Gan (73.5°E), model geometry includes numerous islands which affect the flow; this area is more active in terms of eddies and oscillations. Because of these natural distinctions, we will use the Maldivian longitude to split the basin

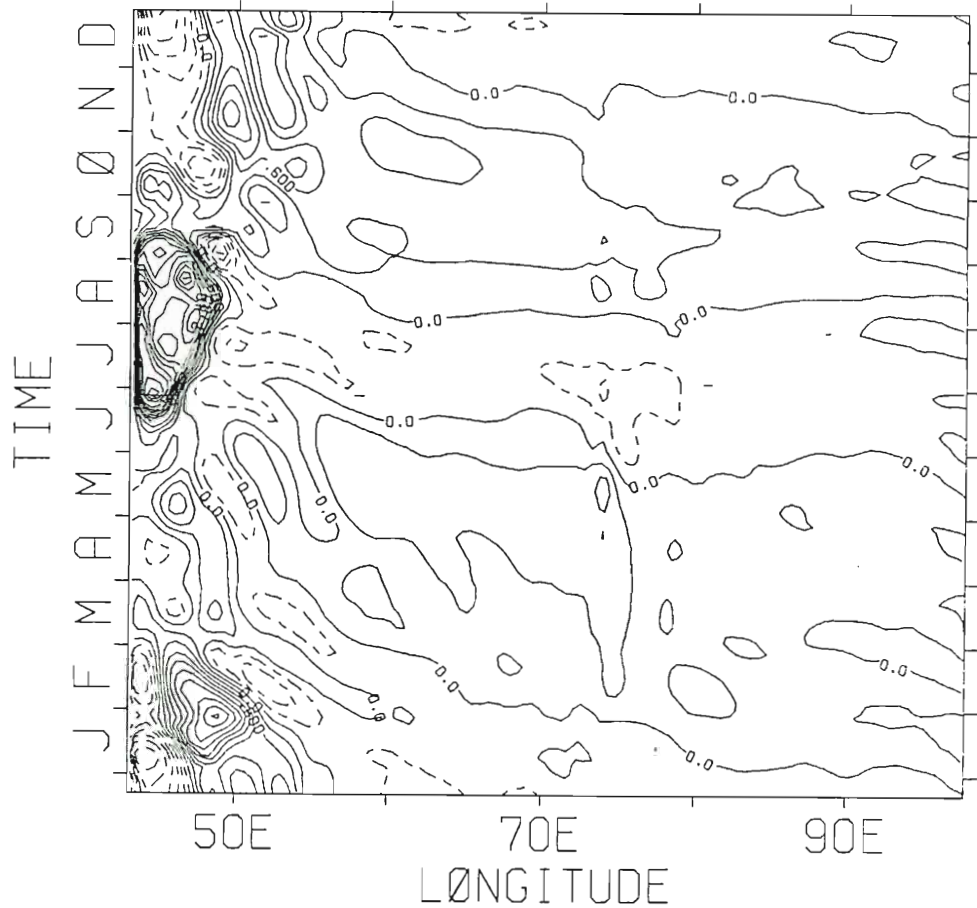


Fig. 17: Longitude-time contours of zonal transport at the equator. Solid (dashed) contours indicate eastward (westward) transport. Between 60°E and 90°E flow is predominantly eastward in February through early June and August through mid-November. Maxima occur in the western basin. Transitions occur generally from east to west except in August. Transport is in Sverdrups ($10^6 \text{ m}^3 \text{ s}^{-1}$) with a contour interval of .3 Sv.

occur in the western basin. Transitions occur generally from east to west except in August. Transport is in Sverdrups ($10^6 \text{ m}^3 \text{ s}^{-1}$) with a contour interval of .3 Sv.

into west and east for the following discussion.

In January the flow west of the Maldives and Gan is westward with weak flow in the east (Fig. 15a). In February, there are two or three weak CCW circulations centered on the western equator with eastward flow dominating in the east. Westerly winds in March cause convergence at the equator generating a downwelling Kelvin wave. Upper layer thickness (ULT) at the eastern boundary increases due to this eastward transport across most of the basin, creating an east-west pressure gradient which balances the wind stress (Fig. 18a). By late May, equatorial flow is blocked by the pressure gradient in the east and splits near 80°E to flow north and south of the equatorial trough (Fig. 18b). The southward flow is geostrophic, ie. along ULT contours. The northern branch of this flow, however, continues essentially eastward at 3° - 5°N at an angle to the ULT gradient. The jet weakens in June such that the wind forcing no longer balances the pressure gradient force and by early July the flow is westward down the pressure (ULT) gradient in the east (Fig. 18c). There is westward flow across the basin by the end of the month. Weak flow in August becomes eastward (Fig. 15c), building the ULT gradient again. A stronger gradient develops north of the equator than south in conjunction with the wind maximum at 5°N . By September, equatorial flow has split near 75°E with stronger flow in the Northern Hemisphere (Fig. 18d). The southern flow stays at the equator for about 5° longitude after the split before turning northern hemisphere (Fig. 18e). The southern flow stays at the equator for about 5° longitude after the split before turning south. It is weaker and breaks down sooner near the equator with a weak eddy forming at the equator east of the Maldives in mid-

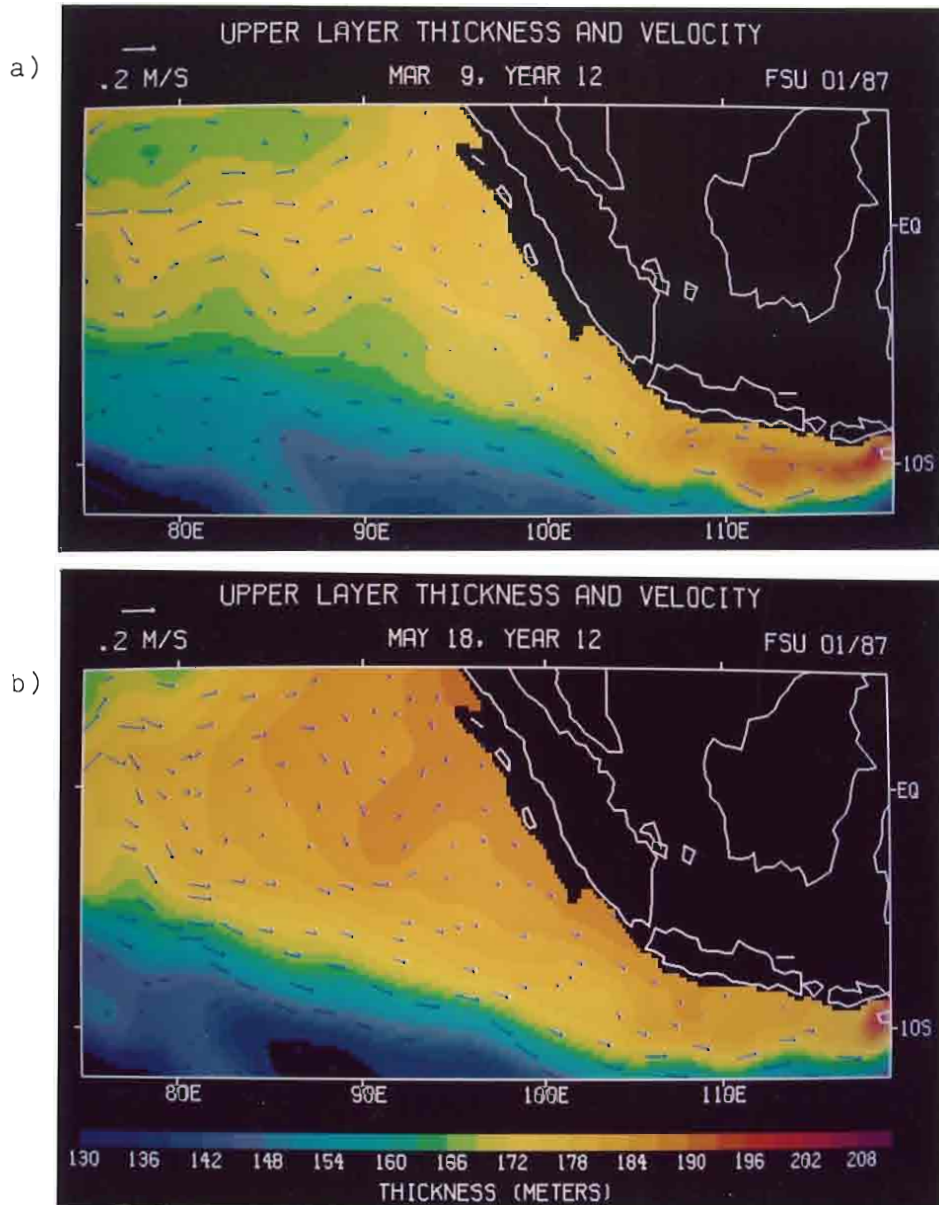
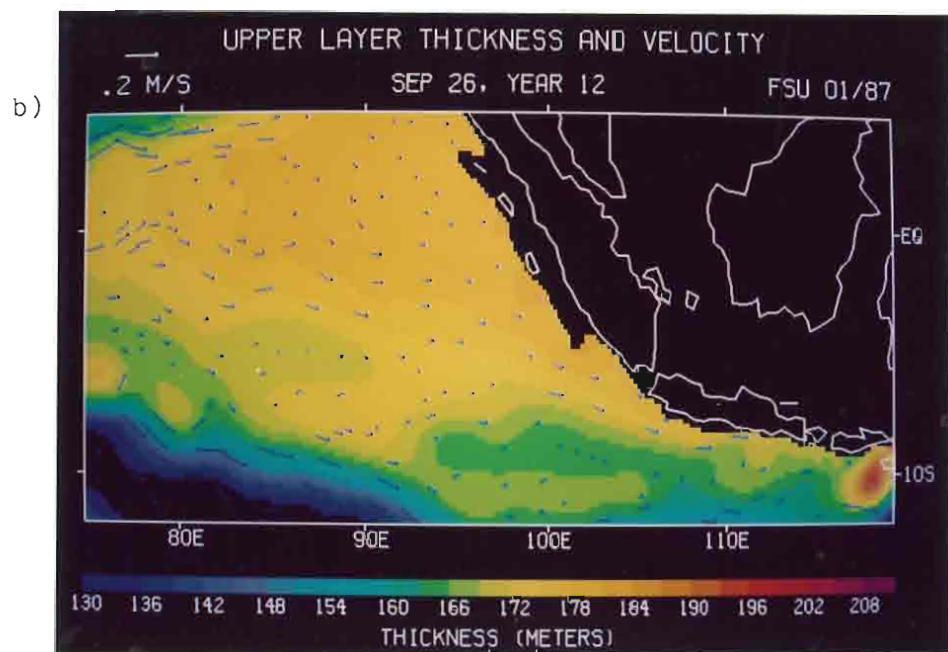
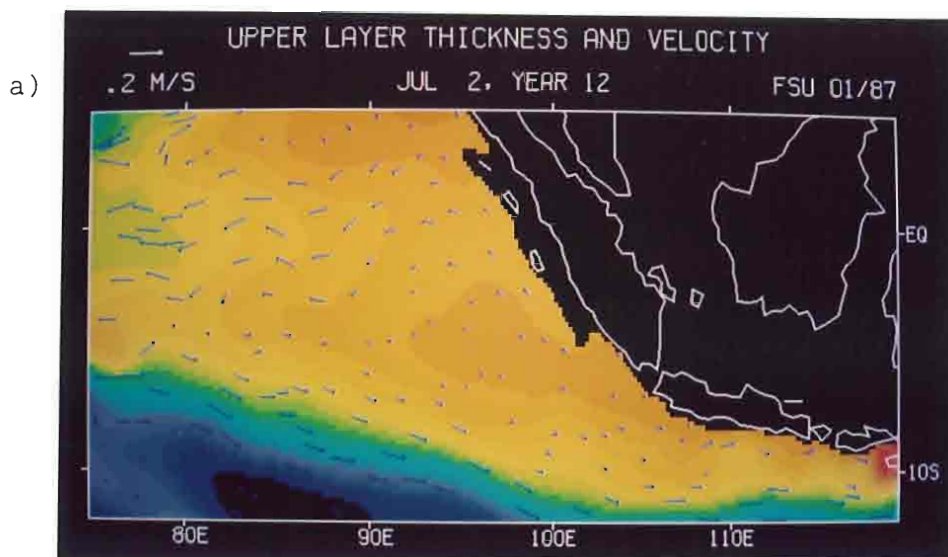


Fig. 18: As in Fig. 13 for the NE quadrant of the domain. Indonesia is in the NE corner.

a) March 9. Eastward equatorial currents and associated downwelling Kelvin waves increase the ULT at the eastern boundary. Coastal Kelvin waves propagate along the Indonesian coast.

b) May 18. Equatorial current splits near 80°E . South of the equator the flow appears geostrophic (along ULT contours) and feeds the SECC. The northern flow continues eastward with large cross equatorial oscillations seen near 90°E as currents (prepare) to reverse to westward.

b) May 18. Equatorial current splits near 80°E . South of the equator the flow appears geostrophic (along ULT contours) and feeds the SECC. The northern flow continues eastward with large cross equatorial oscillations seen near 90°E as currents (prepare) to reverse to westward.



c) July 2. Strong westward flow at equator down the east-west pressure gradient.

c) July 2. Strong westward flow at equator down the east-west pressure gradient.

d) September 26. Equatorial currents have split near 75°E with the southern flow remaining near the equator longer. The ULT gradient is sharper in the north and currents are stronger.

November. Westward flow again appears first in the east and covers the basin to 55°E in December.

One possible reason for the differences in currents in the eastern basin when split into Northern and Southern Hemisphere flows is the asymmetry of the Indonesian coast. The eastward jets are associated with downwelling Kelvin waves at the equator which impinge on the NW-SE slanted boundary. The reflected equatorial Rossby waves are asymmetrical and their effects on the near-eastern boundary region will be asymmetrical. In simple numerical experiments involving the reflection of Kelvin waves at an asymmetrical eastern boundary, the reflected Rossby waves become symmetrical as they move into the ocean interior (T. Jensen, personal communication, 1988). Part of the incoming energy propagates poleward as coastal Kelvin waves which are also asymmetric. The southern wave propagates away from the region. The northern wave follows the closed coastline of the Bay of Bengal. Upon reaching the tip of India it may affect equatorial regions. The passage of the equatorial waves can be seen in the ULT changes in the model.

The SECC is not seen as a continuous current across the basin in the model. Rather, it has several tributaries and is affected by the reversing equatorial currents and by the train of Rossby waves at 12°S . In the western portion of the basin, eastward return flow to the SECC meanders around the banks and islands south of about 4°S when equatorial flow is westward (Fig. 15a). When equatorial the SECC meanders around the banks and islands south of about 4°S when equatorial flow is westward (Fig. 15a). When equatorial currents are eastward, they also feed into the SECC. There are two main tributaries to the SECC. The most continuous flow is 6° - 10°S ,

south of the Seychelles and the Chagos Archipelago. This flow feeds the SECC along the northern edge of Saya de Malha Bank. Fig. 15b shows a second tributary north of the Seychelles and Chagos Archipelago which feeds the SECC farther to the east near 80°E . This tributary is stronger during the SW monsoon than during the NE monsoon as it receives input from the equatorial and Arabian Sea regions during the (northern) summer months. A third return flow is associated with the equatorial and coastal Kelvin wave effects on ULT. Fig. 18d shows this flow along the ULT contours at the Indonesian coast as just described.

There is always some eastward flow at the open section of the eastern boundary in the model simulation. The SECC flows out of the domain at 10° - 13°S (Fig. 19). The Rossby wave zone centers on the open boundary region between Indonesia and Australia with the eastward SECC to the north and westward SEC to the south. Wyrтки's (1987) surface charts show a more northern location for the SEC and recirculation of the SECC into it at 5° - 8°S . Surface observations show predominately westward flow through from the Pacific. Calculations of throughflow also indicate this direction (eg. Wyrтки, 1961; Fine, 1985).

South of the Rossby wave zone at the eastern boundary, a ridge in ULT extends to 22°S early in the year (Fig. 19a). This feature propagates westward to be replaced by a trough in July through September (Fig. 19b). From geostrophic considerations some of the propagates westward to be replaced by a trough in July through September (Fig. 19b). From geostrophic considerations some of the eastward SEC flow bends south and we see poleward flow to about 22°S throughout the year except July through September. This region is of

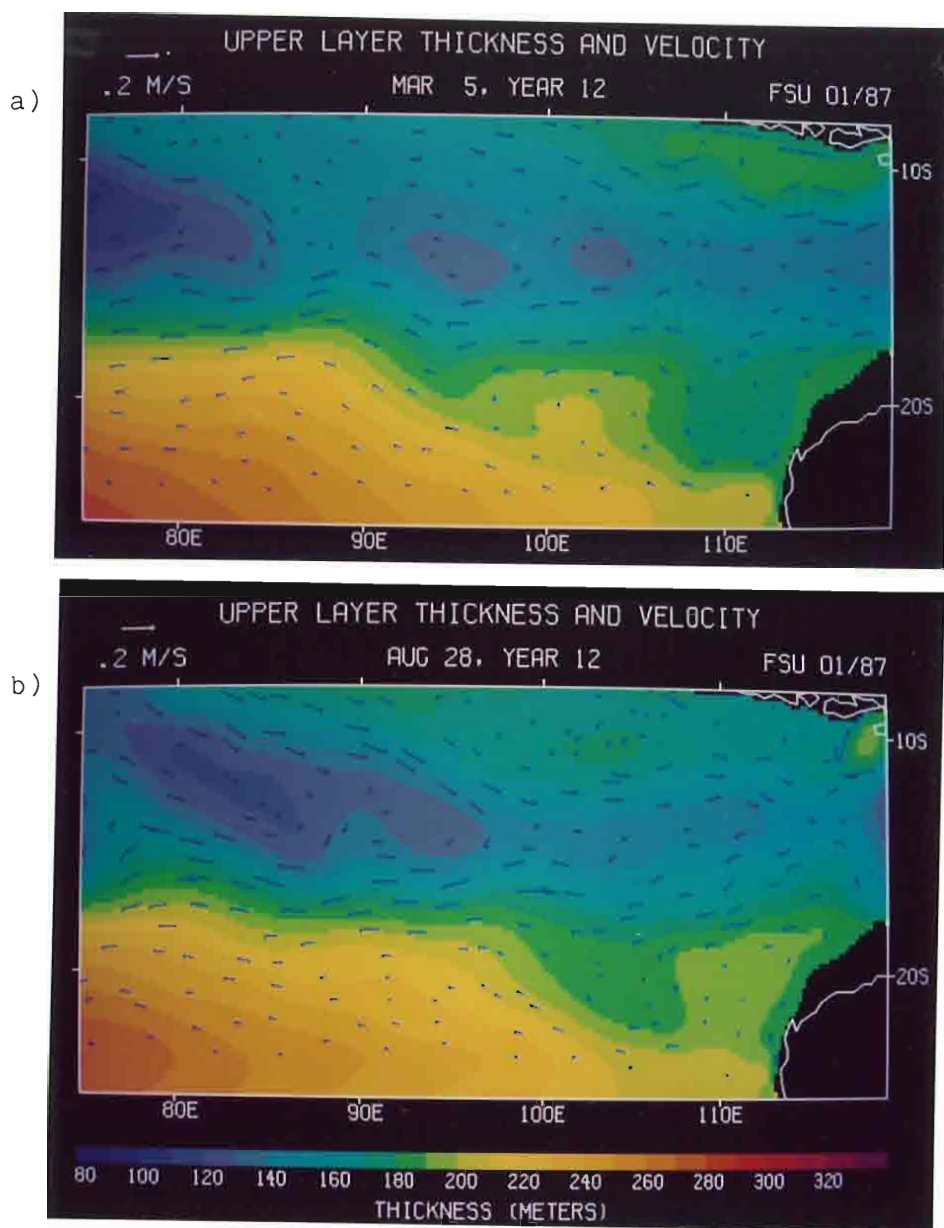


Fig. 19: Same as Fig. 13 for SE quadrant of domain. Australia is in the lower right corner with Indonesia in the upper right.

a) March 5. Several Rossby waves are visible in the SEC-SECC shear zone near 14°S . The SECC does not appear as a continuous zonal flow but rather as a number of tributaries feeding in north of successive Rossby waves. A ridge in the thermocline is present at 110°E with southward flow at the Australia coast.

but rather as a number of tributaries feeding in north of successive Rossby waves. A ridge in the thermocline is present at 110°E with southward flow at the Australia coast.

b) August 28. Rossby waves slanted NW-SE in the west. SECC more continuous over this region at this time. A trough in the thermocline near Australia causes northward flow along the coast.

interest because of the poleward Leeuwin Current observed south of 22°S (Thompson, 1984), the northern limit of poleward flow in the model. We return to this area in a later section.

Fig. 20 summarizes the foregoing discussion. The figure does not represent a particular season, but is instead an attempt at a schematic overview of the large scale circulation in the domain of this study. The northern region of the counterclockwise subtropical gyre is seen along the southern boundary of the domain and is bounded to the north by the SEC. The westward SEC and eastward return flow in tributaries to the SECC define a basin-wide tropical gyre closed in the west by the EACC. This tropical gyre is the most prominent feature of the large scale circulation between the equator and 25°S .

A Rossby wave is generated annually at the eastern boundary and propagates westward in the shear zone between the SEC and SECC. The signal of this wave is found in branches of the SEC through the banks at 60°E and explains the phase difference in the seasonal cycles of the EMC and NMC along the coast of Madagascar. The Seychelles-Mauritius Ridge causes partial reflection of the Rossby wave and an eddy forms due to nonlinear effects in the reflected wave packet. The eddy moves through the break in the banks early in the year and continues westward into the active western boundary region.

The seasonal cycle of the monsoons is most evident in the western boundary region and along the equator. Strong horizontal shears near the African coast between Madagascar and the equator western boundary region and along the equator. Strong horizontal shears near the African coast between Madagascar and the equator cause the formation of CW and CCW eddies. The Somali Current is southward during the NE monsoon, meeting the EACC and turning

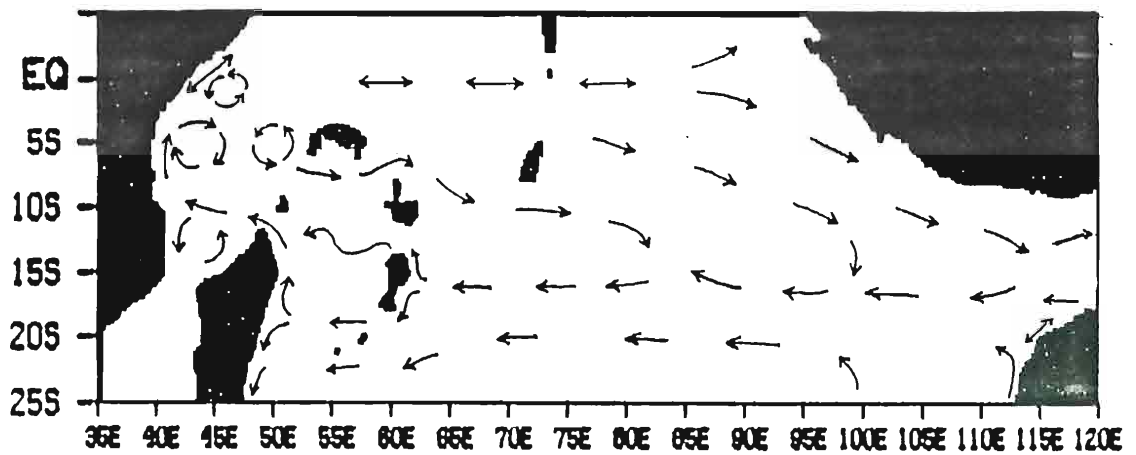


Fig. 20. Schematic diagram of the large scale Southern Hemisphere and equatorial circulation discussed in the text. Double-ended arrows indicate currents which reverse during the year. Current names can be found in the list of abbreviations.

offshore at 2° - 3° S. The CW circulation to the south of this offshore flow develops into the "southern gyre" observed during the SW monsoon when currents are northward along the coast. The gyre is blocked from its often observed northward migration by a CCW eddy which forms in the Northern Hemisphere. The CCW circulation is supported by the southward reversal of the Somali Current with the return of the NW monsoon.

Equatorial currents reverse four times annually with westward flow found near the height of both monsoons and eastward transport found during monsoon transitions. Maximum zonal velocities are found in the western basin with reversals starting generally in the east. Eastward equatorial currents contribute to the SECC which is fed by several tributaries around the islands in the domain.

The ULT field associated with these large scale flows can be interpreted as pressure or dynamic height; that is, high ULT values indicate an elevated dynamic topography. With this interpretation, we see good qualitative agreement with Wyrтки's (1971) and Düing's (1970) maps of geopotential topography. Greatest ULT values are found to the southwest in the center of the subtropical gyre. Flow around the gyre is counterclockwise, following ULT contours with higher values to the left as expected in the Southern Hemisphere (Coriolis parameter, $f < 0$). The gyre expands slightly zonally during February and March, contracts in April through June, expands during July through September, and contracts again in October through February and March, contracts in April through June, expands during July through September, and contracts again in October through January. Meridionally, the gradient sharpens somewhat near the east coast of Madagascar in August through October before relaxing and

remaining fairly constant through the rest of the year (Fig. 13). The ULT is maximum (310m) near southeast Madagascar during the NE monsoon (Fig. 13). A zonal trough of low pressure, ie. thin upper layer, is found north of the gyre between 8°S and 13°S in the west (Fig. 13) and between 10°S and 17°S in the east (Fig. 18). This is a few degrees south of the lows shown by both Wyrтки (1971) and Düing (1970) in topographies referenced to 1000 dbar.

ULT values can also be interpreted as an indication of thermocline depth. Thermocline depth climatologies prepared by Molinari et al. (1986) show a thin upper layer centered at 5°-8°S with thermocline depths on the order of 70-80 m during most of the year. The model ULT also has a minimum value of approximately 80m but toward the center of the gyre model ULT values are about 100m greater than climatological values. Model results are also similar to climatologies prepared by Molinari and Rao (personal communication, 1987).

We have discussed the eddy activity along the African coast north of Madagascar (Fig. 15). Düing (1970) shows patterns of highs and lows in the region which are similar though they are two month averages. The Wyrтки (1971) and Düing (1970) atlases show oscillations in height field at the eastern boundary around the equator which are also suggestive of the thickness variations we see in the model due to the equatorial Kelvin and Rossby waves (Fig. 19).

2. SEC branch transports

in the model due to the equatorial Kelvin and Rossby waves (Fig. 19).

2. SEC branch transports

In the previous section we described the branching of the SEC around Nazareth Bank, at the east coast of Madagascar, and at the

coast of Africa (see Fig. 13). Quadfasel and Swallow (1986) noted that no clear picture has been drawn of how the SEC transport splits into these branches. To address that issue, we calculated transport values for the flows in our model. Latitudes and longitudes were chosen for ease of comparison with observations and another model. We show plots together that refer to the same transect although they may be discussed in different sections of the text. Fig. 3 shows the locations of the transects. A summary of the results is presented in Table 1.

Fig. 21a shows the westward transport in the SEC just east of the Seychelles-Mauritius Ridge (SMR). The current axis is between 16°S and 17°S with values greater than .6 Sv through most of the year. The eddy-like signature from September through February near 12°S is the eddy formed by reflection of the annual Rossby wave contracting before passing through the break in the ridge between 11.5°S and 13.5°S (Fig. 13a). The tongue of westward transport extending to 10°S early in the year is the next Rossby wave reaching north of the blocked eddy. Fig. 21b shows the annual cycle of total westward transport at 63°E between 10°S and 23°S . Mean transport is 24.7 Sv. This is comparable to the results of Godfrey and Golding (1981) who found a zonal jet in mass transport function between 10°S and 15°S with volume transports of 17 Sv at 107°E and 33 Sv at 52°E . The cycle in Fig. 21b is due to the passage of the annual Rossby wave. Maximum westward transport through the break in the SMR at 60°E is found at about 13.2°S (not shown) but shifts to average slightly north of 13°S by 53°E (Fig. 22). Part of the SEC turns to

TABLE 2: Comparison of Madagascar boundary current transports with data calculations and Kindle model.

			Mean Transport
1)	1) Northern tip of Madagascar		
	a) Transect 9 ⁽¹⁾	49°E, 10° - 12°S	16.2 Sv
	b) moorings near 12°S ⁽²⁾	(current axis 313°T) 0 - 200m 0 - 1100m	10.8 Sv 26.9 Sv
	c) mean geostrophic transport ⁽³⁾	0 - 115 km off Cape Amber 0 - 200m	12.6 Sv
	d) Kindle model ⁽²⁾	49°E, 10.4° - 12°S	28.8 Sv
2)	2) Along SE Madagascar		
	a) Transect 6 ⁽¹⁾	22°S, 48° - 50°E	8.2 Sv
	b) moorings near 23°S ⁽²⁾	(current axis 205°T) 0 - 200m 0 - 1100m	7.0 Sv 20.3 Sv
	c) mean geostrophic transport ⁽³⁾	9 - 110 km offshore at 23°S 0 - 200m	7.4 Sv
	d) Kindle model ⁽²⁾	23°S, 48° - 49.6°E	16.5 Sv

(1) this study

(2) Schott et al., 1988

(3) Swallow et al., 1988

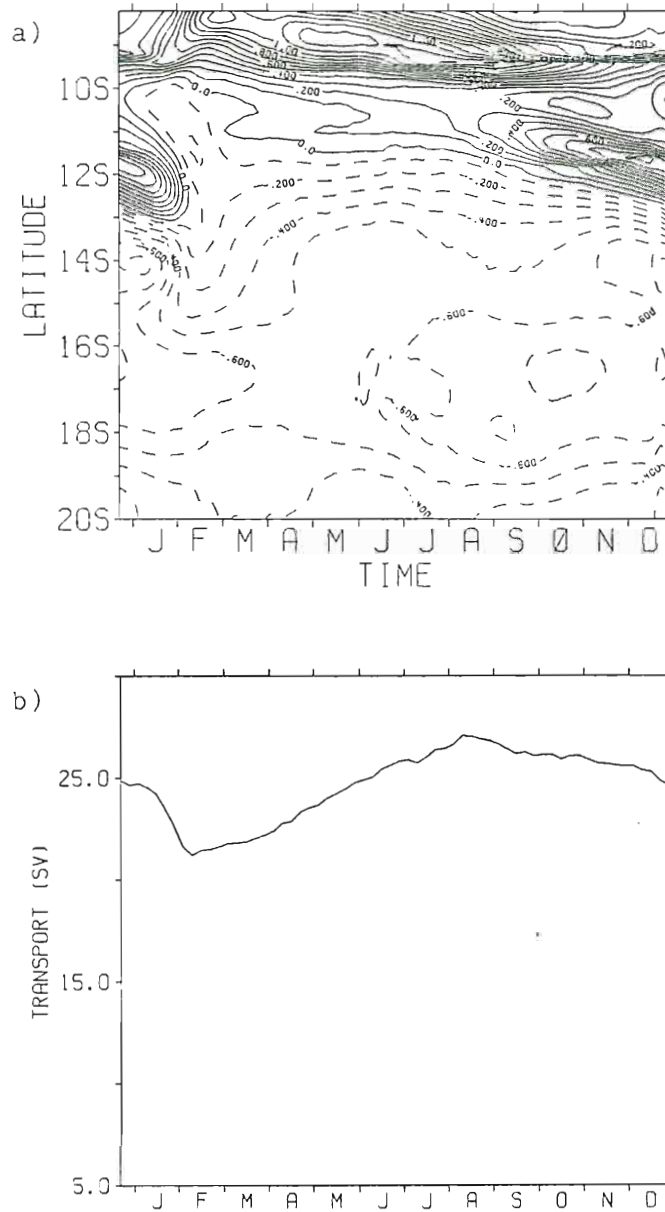


Fig. 21: Zonal transport in the SEC and Rossby wave zone at 63°E , 8° - 20°S . a) Latitude-time contours. Solid (dashed) lines show eastward (westward) transport. The shallow banks along the Seychelles-Mauritius Ridge are located just west of this transect at 60°E . The SECC is seen north of 10°S . Transport units are Sverdrups ($10^6 \text{ m}^3 \text{ s}^{-1}$); contour interval is .1 Sv. b) Total westward transport in the SEC at 63°E , 10° - 23°S . The annual Rossby wave dominates the seasonal cycle.

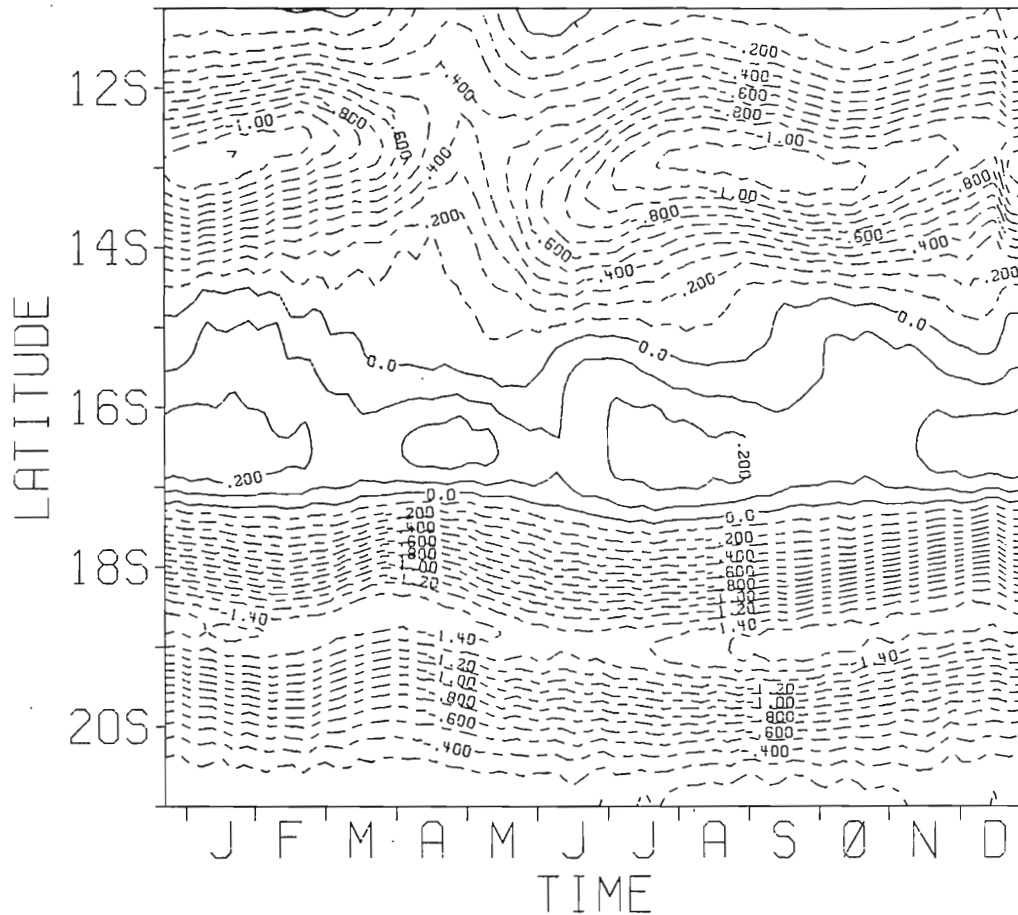


Fig. 22: Latitude-time contours of zonal transport across 53°E in the band $11^\circ\text{S} - 21^\circ\text{S}$. Solid (dashed) contours denote eastward (westward) flow. The two branches of the SEC impinging on the coast of Madagascar are visible at $11^\circ - 15^\circ\text{S}$ and $17^\circ - 21^\circ\text{S}$. Maxima in the northern branch occur in January through February and July through October. The southern branch shows maximum transport in September through January. Some slight eastward flow is observed in the shadow of the shallow banks of the Seychelles-Mauritius Ridge at 60°E . Transport is in Sverdrups ($10^6 \text{ m}^3 \text{ s}^{-1}$) with a contour interval of .1 Sv.

the shadow of the shallow banks of the Seychelles-Mauritius Ridge at 60°E . Transport is in Sverdrups ($10^6 \text{ m}^3 \text{ s}^{-1}$) with a contour interval of .1 Sv.

flow around the south end of the bank with maximum flow at about 18.7°S . The figure shows some slight north-south migrations of the maxima in both flows.

The meridional transport in the northern flow at 12°S clearly shows the westward propagation of the Rossby wave eddy remnant (Fig. 23a). The phase speed calculated from the figure is 9.3 cm s^{-1} which is the same as that calculated for the Rossby waves in Fig. 14a.

The southern branch of the SEC near 19°S impinges on the coast of Madagascar and splits into the southward EMC and northward NMC at the approximate latitude of the current maximum. This is about 2° south of the observed split at 17°S (Schott et al., 1988). The Madagascar boundary currents have equal mean transports of about 8 Sv with seasonal range of about 3.5 Sv (about 40% of the mean flow). The seasonal cycles are shown together in Fig. 24 and are out-of-phase. Comparison of this figure with Fig. 22 shows the May maximum in the northward NMC to correspond with a southward shift in the axis of zonal flow near 19°S as westward flow decreases. Conversely, the southward EMC is maximum as the westward flow axis shifts northward with maximum transport values in November.

This cycle is evident in the gradients of upper layer thickness (ULT). The gradient across the northern branch of the current steepens in May as contours of ULT thickness push northward and the radius of curvature increases. Similar changes occur in the gradient south of 19°S around November as the subtropical gyre deepens. Meridional oscillations in the zonal current reaching the coast are

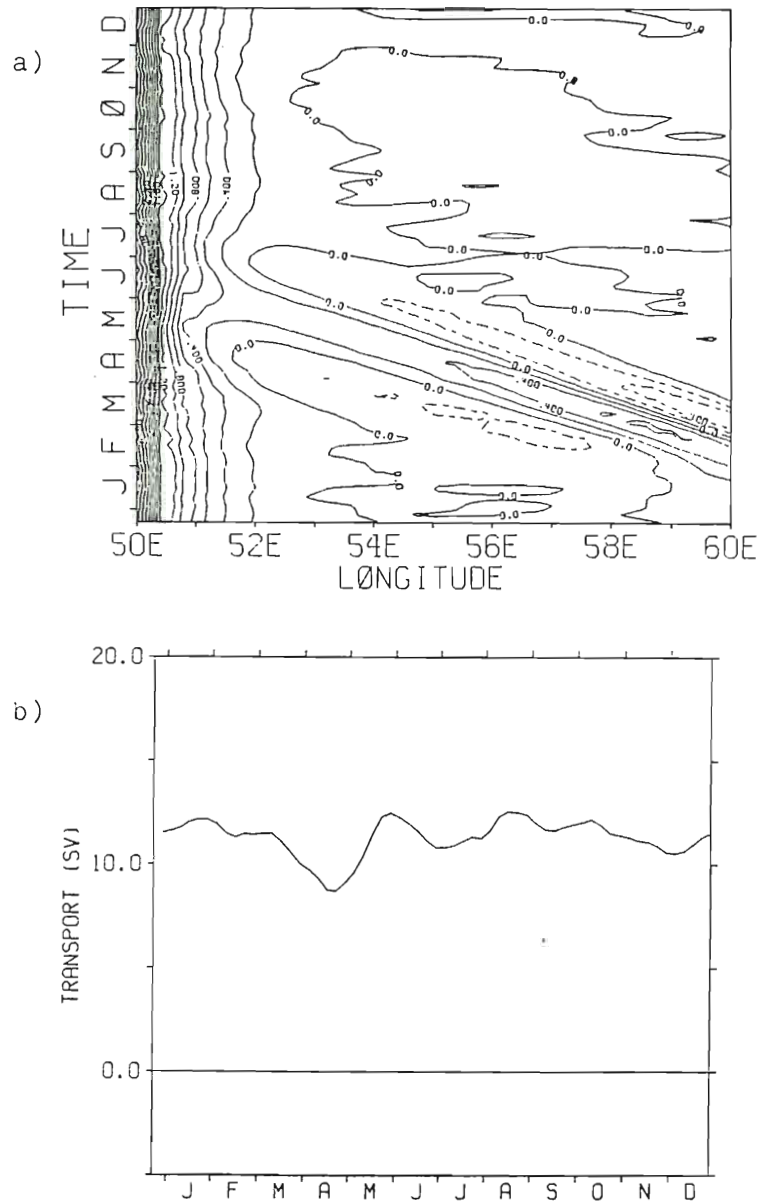


Fig. 23: Meridional transport at 12°S. a) Longitude-time contours from 50°E to 60°E. Solid (dashed) lines indicate northward (southward) transport. Rossby wave trapped east of the Seychelles-Mauritius Ridge at 60°E is seen to propagate westward as an eddy until it is absorbed into the northward current. There is no apparent seasonal cycle in the strong current close to the coast. Transport is in Sverdrups ($10^6 \text{ m}^3 \text{ s}^{-1}$) with contour interval of .2 Sv. b) Smoothed (single pass of 1-2-1 Hanning) annual cycle between 50°E and 53°E. This includes most of the flow that rounds the tip of Madagascar. Mean transport is 11.3 Sv, with seasonal range of 4.3 Sv.

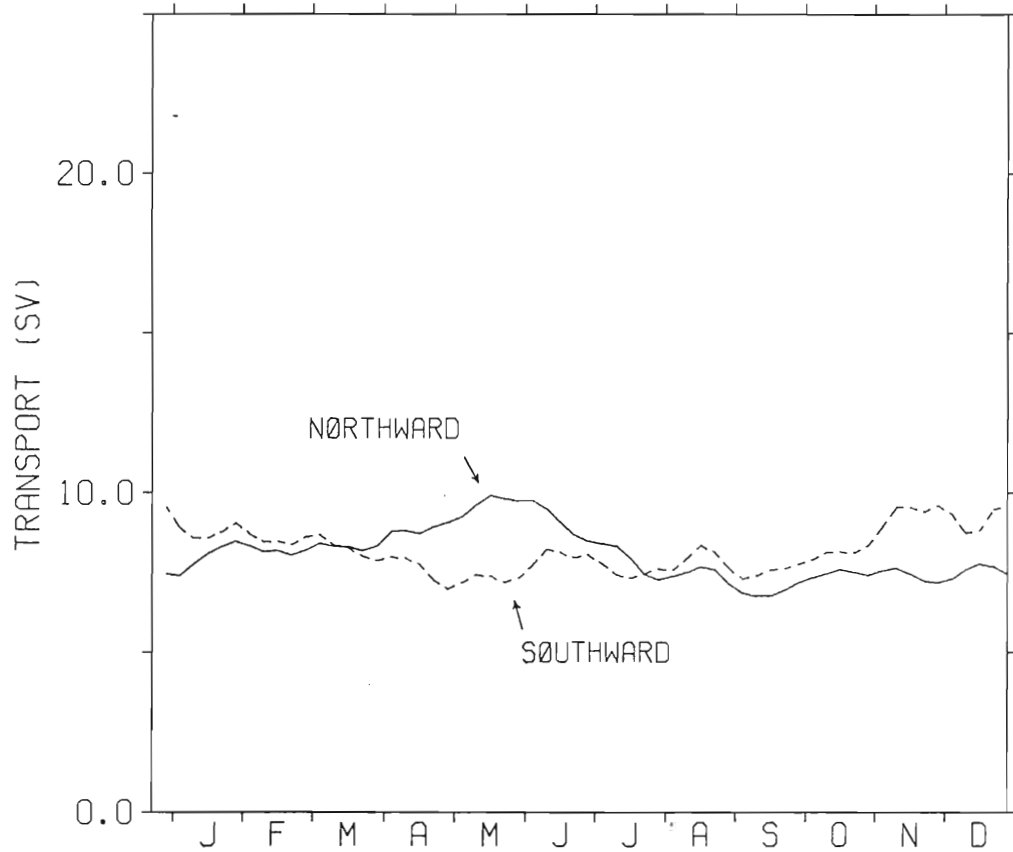


Fig. 24: Meridional transport in East Madagascar Current and Northeast Madagascar Current. Mean northward transport at 16°S , $50^{\circ} - 52^{\circ}\text{E}$ is 8.1 Sv. Seasonal cycle shows a maximum in May and a minimum in September. Mean southward transport at 22°S , $48^{\circ} - 50^{\circ}\text{E}$ is 8.2 Sv. Seasonal cycle shows maxima in November - December and a minimum in late April. Seasonal range in both currents is about 3.5 Sv or about 40% of the mean flow. Both transects have been smoothed using a single pass of a 1-2-1 Hanning filter. Note that current transports are out-of-phase in their seasonal cycles but in-phase at a higher frequency (approximate period of 30-33 days).

evident in Fig. 25a. This transect is just south of the axis of maximum transport as seen by the southward flow (EMC) at 50°E. Maximum northward flow due to the oscillations reaches the coast in May-June when we see the peak northward flow in the NMC (Fig. 24). Southward flow (or reduced northward flow in transects slightly further north, not shown) reaches the coast in November-December when the maximum appears in the southward EMC. We note the similarity between the oscillations in this flow and that at 12°S (Figs. 25a, 23a). The oscillations in the southern branch have an order of magnitude smaller amplitude, but the timing and phase speed are similar to those in the northern branch (8.9 cm s^{-1} at 19°S, 9.3 cm s^{-1} at 12°S). The northern oscillations are clearly related to the Rossby wave signal and we attribute the southern oscillations to the same mechanism. The phase difference between the EMC and NMC, then, is traceable to remote forcing by Rossby waves generated in the eastern basin.

Local wind stress curl may be a factor in the phase shift but it is difficult to see a seasonal cycle in monthly curl fields that explains the current fluctuations. Part of the difficulty may lie in the patchiness of the fields as previously discussed. Within a 2° longitude band of the coast there is generally negative curl in December through April. This should contribute to upward Ekman pumping which would decrease the thickness gradient all along the coast. The pattern in May is strongly positive to the north but with pumping which would decrease the thickness gradient all along the coast. The pattern in May is strongly positive to the north but with negative curl still present south of 20°S in a band of about 1° width. The corresponding downward Ekman pumping in the north might

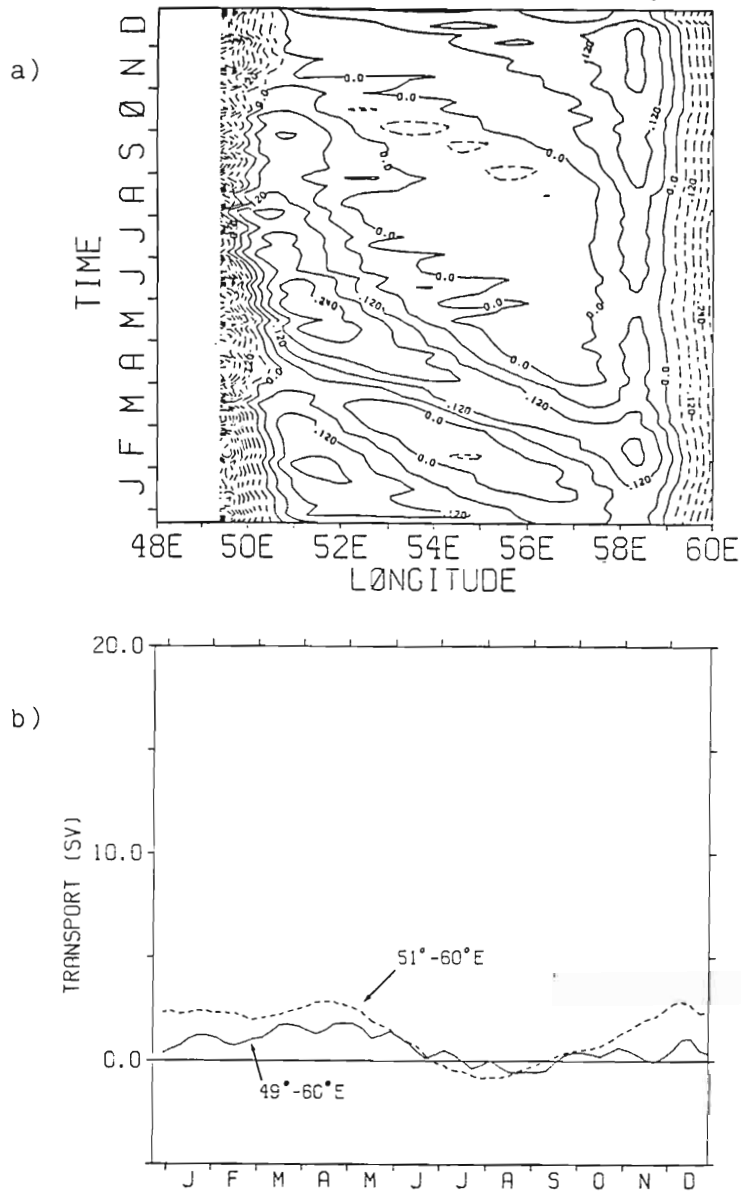


Fig. 25: Meridional transport at 19°S. a) Longitude-time contours for 49° - 60°E. Solid (dashed) contours indicate northward (southward) flow. Southward flow at 50°E is the EMC. Transport units are Sverdrups ($10^6 \text{ m}^3 \text{ s}^{-1}$) with a contour interval of .06 Sv. b) Annual cycle of total transport across 19°S. Positive (negative) values indicate northward (southward) transport. Solid curve is transport between 49°E and 60°E which includes the EMC. Mean transport is .7 Sv with maximum northward flow in March - May and southward flow seen only in mid-July to mid-September. Oscillations have a period of about 40 days. Dashed curve is transport between 51°E and 60°E which excludes the EMC. Mean transport is 1.4 Sv with maximum northward flow in March - May and southward flow seen only in mid-July to mid-September. Oscillations have a period of about 40 days. Dashed curve is transport between 51°E and 60°E which excludes the EMC. A similar seasonal cycle is evident with a mean transport of 1.4 Sv. The oscillations are absent. Both curves have been smoothed with a single pass of a 1-2-1 Hanning filter.

contribute to the observed gradients and transports seen in May. This curl pattern, however, remains steady through November while the gradients change and the maximum transport switches from the NMC to the EMC. It therefore seems likely that local wind stress curl is not a major factor and that this variability is due primarily to remote forcing.

The local winds themselves are, for the most part, weak easterlies during November through February after which they begin to veer southeasterly in transition to the SW monsoon. Fig. 24 shows equal transport north and south at the coast in July when the winds near Madagascar are maximum.

In the north again, the NMC combines with the westward flow at 13°S before rounding Cape Amber at the northern tip of Madagascar. Fig. 26a shows the westward transport at Cape Amber. Mean transport in this current is 16.2 Sv with the maximum flow at 11.2°S . The seasonal cycle shown in Fig. 26b contains significant oscillations from mid-March through mid-October, which will be discussed later.

Schott et al. (1988) present transport calculations from current meter moorings at 12°S and at 23°S . Swallow et al. (1988) estimated mean geostrophic transports from hydrographic sections in the same region. Table 2 compares their findings with our results from similar transects (Figs. 26, 24).

The Schott moorings at Cape Amber were located between 11°S and 12°S . Transports were calculated parallel to the main current axis

The Schott moorings at Cape Amber were located between 11°S and 12°S . Transports were calculated parallel to the main current axis of 313°T . Schott et al. (1988) calculated a value of 10.8 Sv for the top 200 m, noting that their horizontal length scales do not include

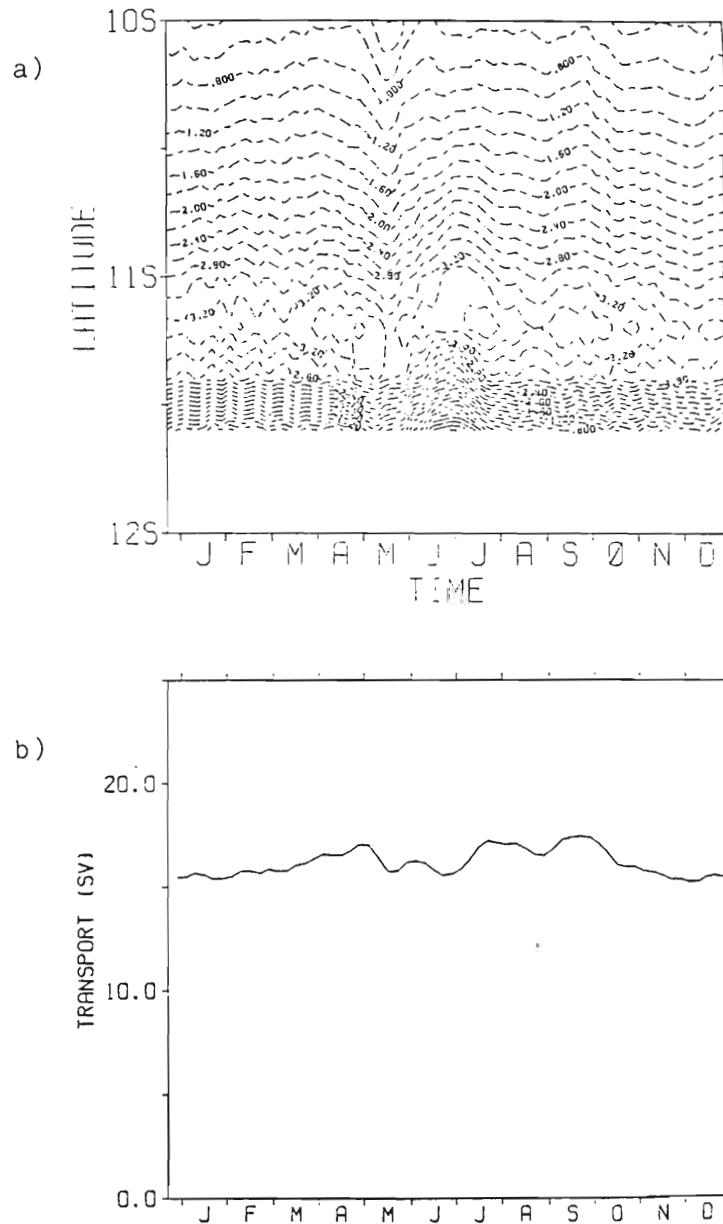


Fig. 26: Westward transport at 49°E, 10°S - 11.6°S. a) Latitude-time contours. The blank area of the figure is the tip of Madagascar extending to 11.6°S. Maximum transport is at 11.2°S with peak values greater than 3.60 Sv. Contour interval is .2 Sv. b) Total transport vs. time. The curve has been smoothed using a single pass of a 1-2-1 Hanning filter. Mean transport is 16.2 Sv. Oscillations occur from mid-March to mid-October with a period of 40 - 50 days. transport vs. time. The curve has been smoothed using a single pass of a 1-2-1 Hanning filter. Mean transport is 16.2 Sv. Oscillations occur from mid-March to mid-October with a period of 40 - 50 days. Peaks correspond to contours of maximum transport in (a).

all of the current through the region. With ULT values near 200 m in the region, we calculate a comparable transport of 16.2 Sv. We note also that there is some westward flow not included in our transect north of 10°S (see Fig. 26a) part of which is due to clockwise recirculation in the lee of the Farquhar group of islands and shoals at 51°E, 10°S, northeast of Cape Amber.

The transport time series from the moorings show no measureable seasonal signal between 150 m and 1100 m depth. In agreement with this, we note the lack of any seasonal signal in the meridional transport at 12°S between 50°E and 51°E in Fig. 23a which constitutes a major portion of the transport through the area of the current meter array of Schott et al. (1988). The annual Rossby wave affects the meridional transport between 50°E and 53°E (Fig. 23b). Swallow et al. (1988) conclude on the basis of shallow hydrography and historical ship drifts off North Madagascar that there may indeed be a seasonal variation of ± 2 Sv with a maximum in August-September and a minimum in January-February. The signal appears to be trapped in the surface layer above the moored array analyzed by Schott et al. Fig. 26b suggests a seasonal cycle with a primary maximum in September and relatively constant flow during November through February. Transport range is 15.0 - 17.8 Sv with aforementioned mean of 16.2 Sv. The winds have a significant seasonal cycle over the ocean east of Madagascar (Hellerman and Rosenstein, 1983; Breidenbach, 1988) which would lead us to expect some seasonal ocean east of Madagascar (Hellerman and Rosenstein, 1983; Breidenbach, 1988) which would lead us to expect some seasonal variability in the currents of the region.

The current axis for the second array of current meters was 25°T

at 23°S. We considered our transect at 22°S which has a mean transport of 8.2 Sv. This is in agreement with the values of 7.0 Sv and 7.4 Sv calculated by Schott et al. (1988) and Swallow et al. (1988) as shown in Table 2. Our Fig. 24 bears no resemblance to the seasonal cycle which Schott et al. describe for 0-1100 m transport.

The reduced-gravity model of Kindle is also forced by the Hellerman-Rosenstein climatology and produces flows which are very similar to ours (Schott et al., 1988). Transport values from that model compare well with those calculated over the entire depth (0-1100 m) of the current meter array (Table 2). They are larger than ours as that model's mean ULT values are greater. Fig. 7 of Schott et al. (1988), shows the model solution for August. Considering an initial thickness of 250 m (our $H_0=200$ m) the ULT values are about 100 m greater than ours which leads naturally to greater transports if velocities are the same. Some adjustment for this should give us comparable transports. Schott et al. note a negligible seasonal cycle in Kindle's model.

Returning to the northern flows, we did a final calculation of mean transport in the EACC at 8.2°S, obtaining a value of 16.3 Sv. There is a great deal of recirculation into the boundary current from the eddies described earlier. As the transport at 8.2°S is the same as that in the zonal current at Cape Amber (16.2 Sv), we suggest that the amount of water recirculating south of that latitude is approximately equal to that which turns south into the Mozambique Channel. Summing the transports in relevant currents gives good results for continuity into and out of this region of branching

Table 1: Transport in SEC branch currents.
Locations are marked in Fig. 3.

Trans	Transect	Transect Location	Transport Direction	Mean Transport	Annual Range	Period of Oscillations
1	1	115°E, 9°-20°S	zonal	.4 Sv	-3.7 - 3.9	30 d.
2	2	63°E, 10°-23°S	westward	24.7 Sv	21.2 - 27.1	---
3	3	61°E, 11°-14°S	westward	7.5 Sv	4.7 - 8.7	---
4	4	60°E, 18°-23°S	westward	16.1 Sv	14.6 - 17.7	---
5	5	19°S, 48°-60°E	meridional	.7 Sv	-.8 - 2.2	30-40 d.
6	6	22°S, 48°-50°E	southward	8.2 Sv	6.8 - 10.1	30 d.
7	7	16°S, 50°-52°E	northward	8.1 Sv	6.5 - 10.2	33 d.
8	8	12°S, 50°-53°E	meridional	11.3 Sv	8.4 - 12.7	60 d.
9	9	49°E, 10°-12°S	westward	16.2 Sv	15.0 - 17.8	40-50 d.
10	10	8.2°S, 40°-43°E	northward	16.3 Sv	11.8 - 21.5	50 d.

flows.

3. Eastern boundary throughflow

There have been many attempts made to estimate the volume of water that flows between the Pacific and Indian Oceans. Wyrтки's (1971) maps of mass transport function in the top 300m relative to 1000 db show that most of the SEC west of 110°E flows into the Indian Ocean through channels between the Indonesian islands. This westward direction of flow is generally accepted but transport values vary widely. The average of all estimates is 9.2 Sv (Gordon, 1986). Wyrтки (1961) was the first to use observations, calculating a transport of 2 Sv in the upper 200m. Godfrey and Golding (1981) estimated a flow of 17 Sv at 107°E from calculations of mass transport function. After considering the Sverdrup flow and boundary current transports in the Pacific, however, they lowered their estimate of throughflow to order 10 Sv as the residual of the Pacific flows. Piola and Gordon (1984) calculated a flow of 14 Sv after a consideration of the salinity budgets in the two oceans. Fine (1985) calculated a throughflow of 5 Sv in the upper 300m using bomb-produced tritium data as evidence of transport. These data also showed the essentially zonal nature of the throughflow across the Indian Ocean.

The throughflow which we can calculate from our model results is only the transport at the open eastern boundary (120°E, 10°-20°S) that is required by internal Indian Ocean dynamics as forced by the winds over the ocean basin. From a transect at 115°E we calculate a mean transport of 0.4 Sv eastward out of the Indian Ocean (Table

1). The direction and small magnitude are not really surprising when we consider that our current system is located slightly southward of its observed position. The SECC is simulated as a significant eastward flow at the eastern boundary, balancing the westward SEC instead of recirculating into it at 5° - 8° S (Figs. 19, 27a).

The observed westward direction of throughflow indicates a gradient between the Pacific and Indian Ocean basins which is not realized in a consideration of the wind-forced Indian Ocean alone. Sea level data indicates a pressure gradient supporting westward flow (Wyrтки, 1987). Schott et al. (1988) conclude that the Indian Ocean wind forcing supplies adequate explanation for the mean transport in the western basin. The throughflow is simulated closer to calculated estimates, however, by general circulation models (GCM) which include Pacific Ocean dynamics. Schott et al. (1988) describe two such models which indicate a throughflow of order 10 Sv. The suggested annual cycle has an amplitude of ± 5 Sv with a maximum in June through August and minimum in January and February. This agrees with the observed sea level gradient between Davao in the Phillipines and Darwin in Australia which is maximum during July and August and near zero during January and February (Wyrтки, 1987). Sea level in the eastern Indian Ocean is the major determinant of the sea level gradient. The seasonal cycle of transport in our model simulation (Fig. 27b) can be seen to agree with the GCM throughflow and observed sea level gradient cycles. Wind driven westward flow is maximum in (Fig. 27b) can be seen to agree with the GCM throughflow and observed sea level gradient cycles. Wind driven westward flow is maximum in July and continues through September, contributing to the maximum seen in the GCM cycle. Maximum eastward flow in December leads the

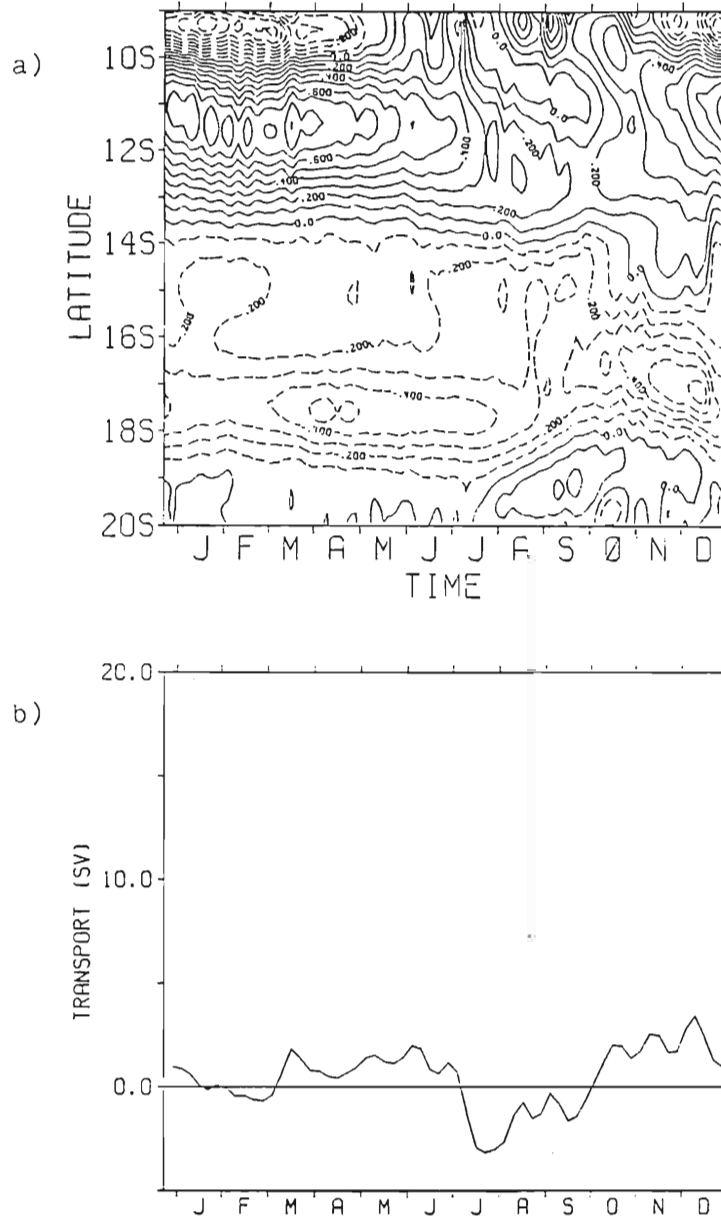


Fig. 27: Eastern boundary throughflow: zonal transport at 115°E. a) Latitude-time contours of transport between Indonesia (9°S) and Australia (20°S) near the model eastern boundary. Solid (dashed) contours indicate eastward (westward) flow. Transport axes of the SEC and SECC are near 17°S and 22°S, respectively. Transport is in Sverdrups ($10^6 \text{ m}^3\text{s}^{-1}$) with a contour interval of .1 Sv. b) Annual cycle of throughflow. Mean transport is .4 Sv eastward with westward (negative) transport in February and July through September. Smoothed curve (single pass of a 1-2-1 Hanning) shows 36-day period oscillations. We note that periods of net eastward transport correlate well visually with maxima in the westward SEC as seen in (a).

GCM minimum westward flow by one month.

4. Transport variability

Several studies have noted a low-frequency variability in the currents of the western Indian Ocean. Mysak and Mertz (1984) found a 40-60 day oscillation in the longshore currents at the African coast between the equator and 5°S. Quadfasel and Swallow (1986) reported 50-day waves in current meter records off the northern tip of Madagascar and similar oscillations in surface currents along a transect at 11°S west of Madagascar. It was suggested that these oceanic oscillations were being forced by the 40-50 day oscillation reported in the tropical atmosphere by Madden and Julian (1972) and found in winds over the western Indian Ocean in 1976 and 1979 by Mertz and Mysak (1984).

The current meter data discussed in the last section evidenced transport variations in the 40-55 day period which accounted for over 40% of the total transport variance (Schott et al., 1988). The oscillations were also present in the ship measurements of Swallow et al. (1988).

In agreement with observations, but in conflict with the suggested mechanism, both our model and the model of Kindle (Schott et al., 1988) simulate oscillations in the same period band northwest of Madagascar using mean monthly winds as forcing. In addition to the oscillations in the EACC and at the northern tip of Madagascar noted earlier, we find oscillations in a 30-60 day band in several the oscillations in the EACC and at the northern tip of Madagascar noted earlier, we find oscillations in a 30-60 day band in several other transects of the Southern Hemisphere flows (Table 1). The highest resolvable frequency in the wind forcing is the Nyquist

frequency of $(2\Delta t)^{-1}$, corresponding to a period of two months. The presence of these higher frequency oscillations in the models requires another mechanism hypothesis. Our model results support the suggestion of Schott et al. (1988) that the oscillations are due to internal instabilities in the ocean. Horizontal shear instability is the only dynamical instability mechanism in this model. The strong horizontal shears throughout the region lead to the formation of eddies through this mechanism.

At the eastern boundary (Fig. 27b), oscillations with an average 36 day period are seen in zonal flow at 115°E . This includes both the SEC and SECC. Also seen is the counterclockwise flow which is present periodically along Indonesia and the small magnitude eastward flow along Australia (Fig. 27a). A transect through the SEC-SECC shear zone shows indications of a similar period oscillation in meridional transport (Fig. 14b). These are somewhat masked by the very strong annual cycle of Rossby wave propagation. Transects farther west across the SEC alone (see Fig. 21b) show no variability in this frequency band but only a strong annual signal. This leads us to speculate that the 30-60 day oscillations at the eastern boundary are advected to the boundary by the eastward return flow from the active eddy region at the African coast. Equatorial and coastal Kelvin waves may contribute to generation and/or advection of these oscillations.

Following our transect series westward, however, the picture of these oscillations.

Following our transect series westward, however, the picture becomes more complicated. The oscillations are absent from the zonal flow following the first split of the SEC at 60°E . As discussed in

Section 4.2, both the northern and southern branches of the flow contain meridional oscillations associated with the annual Rossby wave propagating westward (Figs. 23a, 25a). Total meridional transport associated with the southern flow shows only this seasonal cycle between 51°E and 60°E . When the transect is extended westward to 49°E to include the southward flow in the EMC, however, there are obvious oscillations with an average 36 day period in addition to the seasonal cycle (Fig. 25b). Fig. 24 shows hints of an approximately 40 day oscillation in the meridional transports of both the EMC and NMC.

The pattern changes again in the zonal current at the tip of Madagascar. At 49°E , 40-50 day oscillations are present only in mid-March through mid-October (Fig. 26b). Kindle found transport variations with periods of 70-90 days associated with westward eddy propagation past Cape Amber (Schott et al., 1988). We noted earlier a 70 day period in meridional velocities east of Cape Amber due to the Rossby wave-eddy feature (Fig. 23a). Quadfasel and Swallow (1986) analyzed data records from north and west of Madagascar during March through July, 1975, and found a 50 day period which they attributed to a barotropic Rossby wave. The analysis of Schott et al. (1988) found the oscillations to exist in a yearlong record.

The largest amplitude oscillations in this series of branching flows are found in the strong shear flows in the EACC at the western boundary (Fig. 28b). The period there is about 50 days in agreement with the observations of Mysak and Mertz (1984). Their data was collected about 5° further north during January through July, 1976,

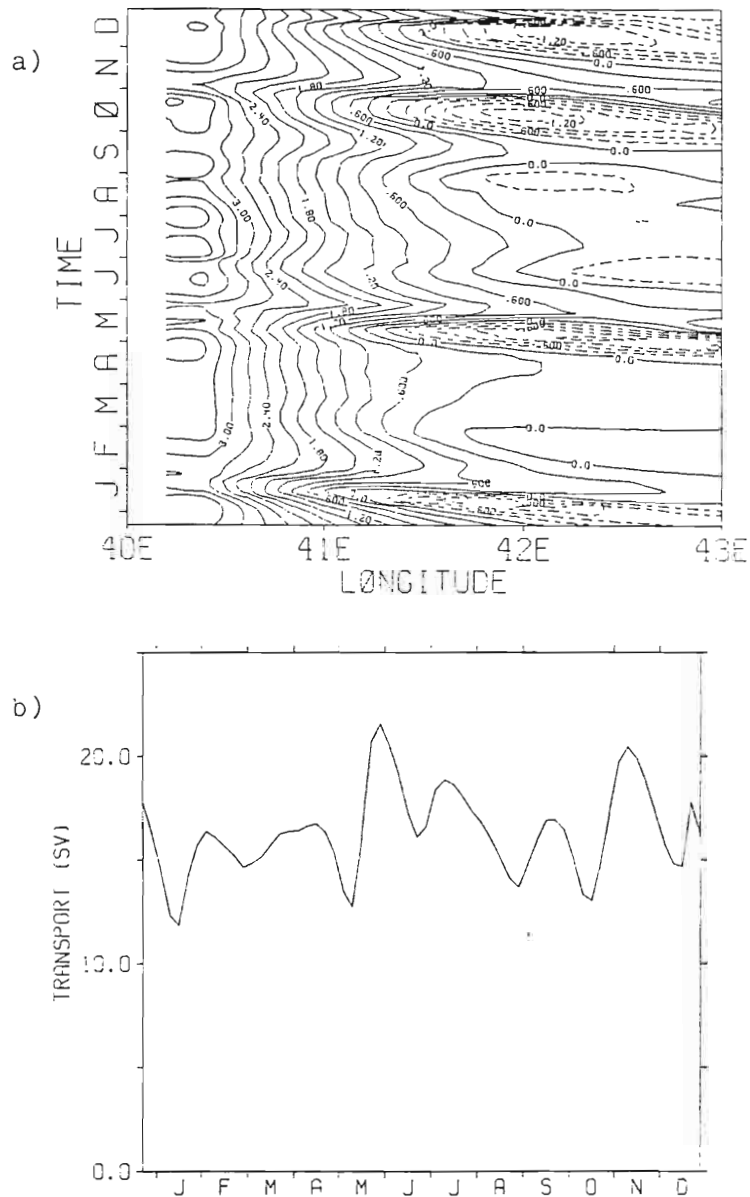


Fig. 28: Meridional transport in the East African Coastal Current at 8.2°S, 40° - 43°E. a) Longitude-time contours. The blank region near 40°E is the African coast. Solid (dashed) contours show northward (southward) transport. Strong eddy activity seen four times during the year from 41°E to 43°E with three additional eddies suggested. Grid noise is evident along the coast. Transport is in Sverdrups ($10^6 \text{ m}^3 \text{ s}^{-1}$) with a contour interval of .3 Sv. b) Total northward transport. Mean transport is 16.3 Sv. Maxima in May/June and in November hint at a seasonal cycle in phase with the onset of the SW and NE monsoons, respectively. The minimum in January is almost matched by those which immediately precede the maxima. Peaks show an oscillation with a period of about 50 days.

covering the NE to SW monsoon transition and the reversal of the Somali Current. The 40-50 day period appears in model solutions not only in transport variability but also in the appearance of eddies as discussed earlier. Fig. 28a shows eddy activity on the eastern edge of the EACC which is related to the transport variability of that flow. The model equatorial currents appear to feed and flow out of this western eddy region. Zonal currents at Gan (73°E) contain 30-60 day oscillations (McPhaden, 1982) which we have not looked for in this analysis. Equatorial currents are oscillatory across the basin, however, as seen in Figs. 15 and 18.

From our series of transects it is unclear where the variability originates. It may be that 30-60 days is a natural period of oscillation of the system, one that is not necessarily limited to the surface currents as is our model. It is interesting to note that the core of the Equatorial Undercurrent in the Pacific oscillates about the equator with a period also of about 40 days (Moore and Philander, 1977). Madden and Julian (1972) postulate that the 30-60 day atmospheric oscillations may be generated somewhere over the Indian Ocean through convection processes. A natural question arises as to the role of the ocean in forcing the atmosphere. We leave this for further investigations.

Additional oscillations are found at the equator where the vanishing of the Coriolis parameter results in mirrored dynamics in the two hemispheres. Linear wave theory identifies several discrete vanishing of the Coriolis parameter results in mirrored dynamics in the two hemispheres. Linear wave theory identifies several discrete modes of oscillation at the equator (Moore and Philander, 1977). The dispersion relation derived from the linear momentum equations has

solutions which correspond to high frequency gravity waves, low frequency Rossby waves, equatorially trapped Kelvin waves, and the special case of mixed Rossby-gravity (Yanai) waves. These mixed waves behave like Rossby waves at low frequency and like gravity waves at high frequency. Only Kelvin waves and mixed Rossby-gravity waves are allowed at periods between about a week and about a month (McPhaden, 1982).

Fig. 29 shows the cycle of the meridional transport field along the western equator from the African coast to Gan (73°E). Waves are generated several times during the year near the coast out of the eddy activity which has been described there. The oscillations at the end of the year are particularly visible in the velocity fields of the model (Fig. 15d). Fig. 29 shows the westward phase speed (about 20 cm s^{-1} as measured from the wave train in April through June) and eastward group velocity (about 24 cm s^{-1}) of these waves. Zonal wavelength is 500 - 650 km, increasing slightly in the east. The period of the waves decreases eastward in this wave train from about 50 days to about 27 days. Measurements east of 60°E are indicative of mixed Rossby-gravity waves. Further west, however, frequency and wavenumber correspond to that region of the linear dispersion diagram where mixed Rossby-gravity waves are indistinguishable from short Rossby waves which also have westward phase velocity and eastward group velocity. The waves decay eastward possibly due to nonlinear interactions with predominately zonal phase velocity and eastward group velocity. The waves decay eastward possibly due to nonlinear interactions with predominately zonal equatorial currents.

The dominant period in meridional velocity at 55°E is found by

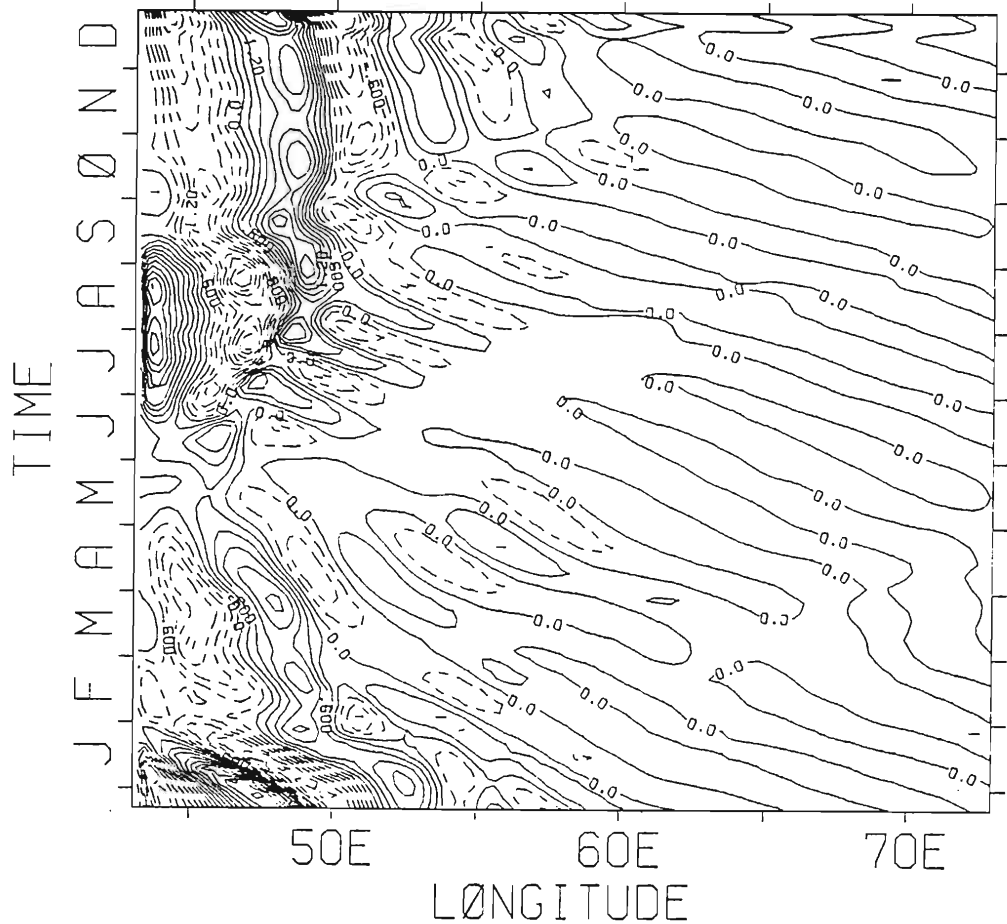


Fig. 29: Time-longitude contours of meridional transport along the equator between the Africa coast and Gan ($43^{\circ} - 73^{\circ}\text{E}$). Solid (dashed) contours show northward (southward) transport. Offshore there is evidence of mixed Rossby-gravity waves with westward phase propagation and eastward group velocity. They are generated near the coast four to five times during the year. Transport is in Sverdrups ($10^6 \text{ m}^3 \text{ s}^{-1}$) with a contour interval of .4 Sv.

propagation and eastward group velocity. They are generated near the coast four to five times during the year. Transport is in Sverdrups ($10^6 \text{ m}^3 \text{ s}^{-1}$) with a contour interval of .4 Sv.

fast Fourier transform methods to be about 40 days with a second peak near 28 days. West of 55°E the semiannual signal becomes very strong but the same two peaks are still visible at 50°E. The dominant period is 33 days at 60°E with a smaller peak near 26 days. At 65°E and 70°E there is a single peak at 28 days, suggesting a mixed Rossby-gravity wave. Luyten and Roemmich (1982) observed a dominant 26 day period in a composite meridional velocity at 200 m from moored current meters between 47°E and 62°E. They attribute the oscillations (wavelength of 1400 km) to mixed Rossby-gravity waves (Luyten and Roemmich, unpublished manuscript). O'Neill (1984) also found characteristics of mixed Rossby-gravity waves in a different array of moorings at 53°E. O'Neill notes that incoming energy is likely to be reflected as mixed Rossby-gravity waves due to the NE-SW angle of the African coast at the equator. Kindle also reports 27-day equatorial oscillations being generated in his model by the "instability of the eastward flow" away from the coast (Schott et al., 1988). While our model results support the conclusion that mixed Rossby-gravity waves may be present, we note the longer period also present in velocity and transport east of about 60°E. This may be a result of the eddy activity to the south or may indicate the reflection of long Rossby waves as short Rossby waves with eastward group velocity.

5. Mozambique Channel

From the northern tip of Madagascar, the model current flows

5. Mozambique Channel

From the northern tip of Madagascar, the model current flows almost due westward. At the coast of Africa roughly 85% of the flow turns northward as the East African Coastal Current (EACC). The

remainder of the the flow turns south into the Mozambique Channel where it contributes to counterclockwise circulation centered at about 12°S (Fig. 13). The most energetic circulations are restricted to the area north of the channel constriction at 16°S . An eddy forms in this northern region approximately monthly from February to October in the central channel and propagates westward to flatten against the African coast (Fig. 13a). During May through July, positive wind stress curl increases west of Cape Amber. The eddies form farther east and augment each other such that the upper layer is 40 m thicker than the surroundings (Fig. 13b); this is twice the increase seen in other months. Beginning in July, the counterclockwise circulation at the African coast extends increasingly southward with contributions from successive eddies in the north. In December and January this shallow trough extends to approximately 21°S (Fig. 13c). The model does not reproduce the Mozambique Current along the African coast and generally shows very little flow in the southern channel. As the model domain extends only to 25°S , there is no allowance for continuity of flow around the southern tip of Madagascar. The wind stress curl over the region is generally negative with positive curl at the African coast during the SW monsoon.

Atlases and charts of surface currents (see Dietrich and Ulrich, 1968; Düing, 1970) show the counterclockwise circulation in the northern channel, but traditionally depict the Mozambique Current as a tributary of the Agulhas Current which flows south around the tip of the African continent. This picture has been questioned in the

past two decades and there is continued uncertainty regarding regional flow patterns (See Satre and da Silva, 1984, and Lutjeharms, 1976, for brief discussions of other studies). The influence of the monsoon seasons in the northern Indian Ocean on the currents in the southern Indian Ocean has been shown (see Lutjeharms, 1976). Soares (1975) concluded that the Mozambique Current does not contribute significantly to the Agulhas Current during the SW monsoon. During the NE monsoon, however, the Mozambique Current may be the major source of water in the upper layers (Lutjeharms, 1976).

Satre and da Silva (1984) analyzed data from 1977 to 1980 off the coast of Mozambique and historical data from the Mozambique Channel. They concluded that the Mozambique Current plays a minor role in supplying the Agulhas Current in the upper 1000m and may not be a continuous current at all. Based on the temperature structure at 150m and the dynamic height relative to 500dbar, they suggest two tentative flow patterns. As a general circulation pattern, they suggest that the channel contains two counterclockwise cells within the domain of our model and a third south of 25°S. Smaller clockwise eddies are located between the larger cells. This pattern applies to the circulation below the surface layer and is likely greatly affected by topography. The second pattern is suggested as a modification of the surface layer by local winds. The two cells north of 25°S are merged so that a somewhat continuous current may exist in that part of the channel. The data support this surface north of 25°S are merged so that a somewhat continuous current may exist in that part of the channel. The data support this surface pattern during the southern winter (SW monsoon), but indicate a separation of the gyres during the southern summer (NE monsoon). Our

model results (which do not include effects of topography) are suggestive of the surface pattern, but, contrary to the conclusions of Satre and da Silva, this circulation is most developed in the southern summer (NE monsoon, Fig. 13c).

It is interesting to note that a version of our model with islands removed does create a southward Mozambique Current along the coast of Africa as shown in atlases. The shallow trough is present during most of the year, extending furthest south in December. A linear version produces weak flows similar to the ones we have described.

6. Western Australia (Leeuwin Current)

The western coast of Australia is a region of interest due to observations of the poleward flowing Leeuwin Current, an anomaly at an eastern boundary. Surface current charts such as those of Wyrski (unpublished manuscript) do show northward flow throughout the year along the northwest coast. The Leeuwin Current, however, flows southward between 22.5°S and 32.5°S during April through October with strongest flow observed in May (Godfrey and Ridgway, 1985). The thermocline is relatively deep along this part of the coast (Thompson, 1984) in keeping with the southward flow, but is again anomalous with respect to the upwelling normally observed at eastern boundaries.

The model simulation in this region is very different from observations. Part of the SEC bends to give weak southward flow

The model simulation in this region is very different from observations. Part of the SEC bends to give weak southward flow along the northwest Australian coast to 22°S during November through July (Fig. 19a). South of this latitude, the model shows only

northward flow where the narrow southward Leeuwin Current has been observed. Negative wind stress curl along the coast in November through March causes Ekman suction and the formation of a ridge in the thermocline. The ridge extends south from the Rossby wave zone to about 22°S forcing the northward flow to turn offshore. West of the ridge the flow turns northward again to join the SEC. Positive curl is established by April with corresponding Ekman pumping beginning to push the thermocline down. The ridge propagates westward, reinforced by negative curl offshore, and is replaced by a trough forming at the coast in late July when positive curl at the coast is strongest. With the trough reaching to about 18°S, flow becomes northward all along the coast (Fig. 19b). Negative curl becomes dominant again during subsequent months and the ULT gradient reverses as suction replaces pumping. Northward flow north of 22°S breaks down in October as a new ridge appears at the coast and southward flow is reestablished. To the west the ridges and troughs are absorbed into the subtropical gyre.

The ridge-trough system travels westward, covering about 5° longitude in four months. This gives a speed of 5 cm s^{-1} at 20° latitude which is very close to the theoretical first baroclinic mode Rossby wave phase speed at that latitude. We interpret this ridge-trough system as an annual Rossby wave generated by the cycle of local wind stress curl.

The alongshore component of the wind does not contribute to the local wind stress curl.

The alongshore component of the wind does not contribute to the ridge-trough system. It actually would seem to counteract the curl-pumping mechanism. Offshore Ekman transport due to the south-

westerlies in November to February, if acting alone, would build a gradient opposite to that observed. Coastal flow at this time is counter to the alongshore wind. The winds back southeasterly, peaking in July, possibly contributing some southward Ekman transport in May through July. The flow becomes northward temporarily as the alongshore winds strengthen again but reverses before they are fully developed southwesterly again.

Near the southern boundary of the model, the curl is negative in November through April, and alongshore winds cause offshore Ekman transport. These local winds contribute to the east-west ULT gradient of the subtropical gyre and the shallow thermocline at the coast which, as mentioned previously, is contrary to observations.

At least one of the reasons for the discrepancies between our model results and observations is likely the use of wind stress alone as forcing for the model. Other studies have investigated throughflow of low-density water from the Pacific (Godfrey and Golding, 1981; Godfrey and Ridgway, 1985; Kundu and McCreary, 1986) and thermohaline forcing (McCreary et al., 1986) as contributors to the formation of a poleward eastern boundary current and the lack of upwelling. McCreary et al. (1986) obtain good agreement with observations using combined thermohaline and wind forcing. Remote forcing by Pacific throughflow may still contribute, however, as not all aspects of their model response agree with observations.

all aspects of their model response agree with observations.

IV. DISCUSSION

The FSU Indian Ocean model, driven by the climatological monthly mean winds of Hellerman and Rosenstein (1983), accurately simulates the major features of the large scale upper ocean circulation in the Southern Hemisphere and equatorial regions. Major currents (SEC, SECC, EACC, Somali Current) are found close to their observed locations. Mean transports in the western basin are comparable to observations. The principal feature of the circulation in the Southern Hemisphere tropical Indian Ocean is a basin-wide clockwise (cyclonic) gyre comprised of the SEC in the south, the SECC to the north and the EACC in the west. The western boundary region of this tropical gyre is a source of energetic eddy activity that is generated through shear instabilities. The "southern gyre" of the (northern) summer Somali Current is seen as a northward extension of the western boundary current of this tropical gyre, and appears to be a tropical analog to the Gulf Stream recirculation region of the North Atlantic subtropical gyre. Outflow from this region meanders eastward through various tributaries to the SECC and then into the Sverdrup-like interior.

The Southern Hemisphere gyre is the steady response of the ocean to the mean basin-wide wind stress curl distribution, and exhibits most of the features of a classical mid-latitude gyre, modified by its proximity to the equatorial waveguide and by the large seasonal

most of the features of a classical mid-latitude gyre, modified by its proximity to the equatorial waveguide and by the large seasonal

variability in the wind fields. The response of the ocean interior is therefore an important determinant of the western boundary flow. The negative wind stress curl over the interior region of the southern ($f < 0$) tropical gyre causes upward Ekman pumping, thereby squashing vortex tubes and requiring that they move poleward to conserve potential vorticity. Equatorward flow at the western boundary provides for mass conservation and restoration of potential vorticity to match that of the interior flow. The recirculation region near the western boundary south of the equator, as with that associated with the Gulf Stream, provides additional time in the boundary current for fluid parcels to acquire the necessary potential vorticity to reenter the interior flow. Further discussion of these dynamics can be found in Moore (1963) and in Chapter 5 of Pedlosky (1987).

The tradewinds of the Indian Ocean are significantly different from those of the Atlantic and Pacific. The Southern Hemisphere southeasterly trades are found farther south than in the other oceans and exhibit a strong annual cycle. Tradewinds are found in the Northern Hemisphere only during the NE monsoon, and the reversals of the monsoon winds have no counterpart in area or intensity over other oceans. In comparison, the Pacific and Atlantic are relatively symmetrically forced north and south of the equator although there is also some seasonal variability in their trades. These oceans display major tradewind-driven gyres in both hemispheres. There is also some seasonal variability in their trades. These oceans display major tradewind-driven gyres in both hemispheres. There is a large gyre in the southern subtropical Indian Ocean but no counterpart in the Northern Hemisphere. The equatorial current system during the NE

monsoon is found shifted south of the Atlantic and Pacific systems and our model shows the currents to be part of the tropical gyre discussed above. During the SW monsoon, the observed gyre extends across the equator, encompassing return flow from the Arabian Sea in the SW Monsoon Current.

Model solutions demonstrate the expected wave types at the equator. Downwelling Kelvin waves adjust mass eastward in association with the equatorial jets. Equatorial Rossby waves propagate information westward and affect the circulation at the western boundary. Oscillations with a 28-day period may be either mixed Rossby-gravity waves generated at the western boundary or short reflected Rossby waves with eastward energy propagation. Reflections in the northern and Southern Hemisphere are asymmetric at both eastern and western boundaries due to the opposite slants of the coastlines at the equator. This is an interesting phenomenon which is noted but not investigated in this study.

Most of the currents transected in this study exhibit oscillations in zonal or meridional transport. The annual Rossby wave signal is seen in SEC transports through the Seychelles-Mauritius Ridge and is responsible for the seasonal cycles in the EMC and NMC along the coast of Madagascar. The region of eddy activity northwest of Madagascar is dominated by variability in the 30-60 day period band. The EACC has prominent oscillations with a period of about 50 days. This frequency range is also found in the model period band. The EACC has prominent oscillations with a period of about 50 days. This frequency range is also found in the model solutions of Kindle (Schott et al., 1988) and is in agreement with observations. With 60 days as the shortest resolvable period in the

wind forcing, we attribute the model and observational variability to shear instabilities inherent in the ocean, not to atmospheric forcing as has been suggested by others, since the model has no forcing at those periods.

We have noted regions where the model has some difficulty, namely in the Mozambique Channel (although patterns of flow there are in question) and at the eastern boundary in regards to the Leeuwin Current and Pacific throughflow. Additionally, because of the mean wind stress curl patterns, the major zonal currents which define the tropical gyre are simulated a few degrees south of their observed locations during the NE monsoon and are not significantly altered by southward flow from the Arabian Sea during the SW monsoon.

Additional forcing mechanisms appear to be required for accurate modelling of these regions. The addition of reasonable throughflow forcing to the model would presumably shift the SEC-SECC gyre northward towards its observed location as it would be a major source of water for the SEC. Throughflow also appears to be important for successful simulation of the Leeuwin Current although thermohaline forcing appears to be responsible for the mean circulation with the wind stress forcing the annual variability (McCreary et al., 1986).

The model results are limited by the accuracy of the wind forcing. Observations from the Southern Hemisphere are limited. The model boundaries are also a problem as no flow is allowed to enter the model domain in a region where there is physically a significant model boundaries are also a problem as no flow is allowed to enter the model domain in a region where there is physically a significant input from the south and the east. The placement of the southern boundary at 25°S may be a factor in the circulation simulated in the

Mozambique Channel, as no continuity of flow is allowed around the southern tip of Madagascar in the model.

It is possible to reproduce the large scale features of the southern Indian Ocean with wind forcing alone. The results of this study provide encouragement for further model development. Verification of improvements will require increases in observational data. A combined effort of modellers and observationalists is therefore required for further understanding of the circulation of the southern tropical Indian Ocean.

References

- Anderson, D. L. T., and D. W. Moore, Cross-equatorial inertial jets with special relevance to very remote forcing of the Somali Current, Deep-Sea Res., 26, 1-22, 1979.
- Barnett, T., Interaction of the monsoon and Pacific trade wind system at interannual time scales. Part I: The equatorial zone, Mon. Wea. Rev., 111, 756-773, 1983.
- Breidenbach, J., EOFs of windstress over the Indian Ocean (1977-1985), submitted to the Bull. Amer. Meteor. Soc., 1988.
- Bruce, J. G., Large-scale variations of the Somali Current during the southwest monsoon, 1970, Deep-Sea Res., 20, 837-846, 1973.
- Cadet, D. L., and B. C. Diehl, Interannual variability of surface fields over the Indian Ocean during recent decades, Mon. Wea. Rev., 112, 1921-1935, 1984.
- Camerlengo, A. L., and J. J. O'Brien, Open boundary conditions in rotating fluids, J. Comput. Phys., 35, 12-35, 1980.
- Dietrich, G., and J. Ulrich (Eds.), Atlas zur Ozeanographie, 77 pp., Bibliographisches Institut, Mannheim, 1968.
- Dube, S. K., M. E. Luther, and J. J. O'Brien, Relationships between interannual variability in the Arabian Sea and Indian summer monsoon rainfall, submitted to J. Geophys. Res., 1988.
- Düing, W., The Monsoon Regime of the Currents in the Indian Ocean, 68 pp., East-West Center Press, Honolulu, 1970.
- Düing, W., The Monsoon Regime of the Currents in the Indian Ocean, 68 pp., East-West Center Press, Honolulu, 1970.

- Fine, R., Direct evidence using tritium data for throughflow from the Pacific into the Indian Ocean, Nature, 315, 478-480, 1985.
- Godfrey, J. S., and T. J. Golding, The Sverdrup relation in the Indian Ocean, and the effect of Pacific-Indian Ocean throughflow on Indian Ocean circulation and on the East Australian Current, J. Phys. Oceanogr., 11, 771-779, 1981.
- Godfrey, J. S., and K. R. Ridgway, The large-scale environment of the poleward-flowing Leeuwin Current, Western Australia: longshore steric height gradients, wind stresses and geostrophic flow, J. Phys. Oceanogr., 15, 481-495, 1985.
- Gordon, A. L., Interocean exchange of thermocline water, J. Geophys. Res., 91, 5037-5046, 1986.
- Hellerman, S., and M. Rosenstein, Normal monthly wind stress over the world ocean with error estimates, J. Phys. Oceanogr., 13, 1093-1104, 1983.
- Knox, R. A., On a long series of measurement of Indian Ocean equatorial currents near Addu Atoll, Deep-Sea Res., 23, 211-221, 1976.
- Knox, R. A., and D. L. T. Anderson, Recent advances in the study of the low-latitude ocean circulation, Prog. Oceanogr., 14, 259-318, 1985.
- Kundu, P. K., and J. P. McCreary, Jr., On the dynamics of the throughflow from the Pacific into the Indian Ocean, J. Phys. Oceanogr., 16, 2191-2198, 1986.
- throughflow from the Pacific into the Indian Ocean, J. Phys. Oceanogr., 16, 2191-2198, 1986.

- Luther, M. E., and J. J. O'Brien, A model of the seasonal circulation in the Arabian Sea forced by observed winds, Prog. Oceanogr., 14, 353-385, 1985.
- Luther, M. E., J. J. O'Brien, and A. H. Meng, Morphology of the Somali Current system during the southwest monsoon, in Coupled Ocean-Atmosphere Models, edited by J. C. J. Nihoul, pp. 405-437, Elsevier Science Publishers B. V., Amsterdam, 1985.
- Luther, M. E., Indian Ocean modelling, Further Progress in Equatorial Oceanography, edited by E. Katz and J. Witte, pp. 303-316, Nova Univ. Press, Dania, Florida, 1987.
- Lutjeharms, J. R., N. D. Bang, and C. P. Dugan, Characteristics of the currents east and south of Madagascar, Deep-Sea Res., 28, 879-900, 1981.
- Luyten, J. R., and D. H. Roemmich, Equatorial currents at semi-annual period in the Indian Ocean, J. Phys. Oceanogr., 12, 406-413, 1982.
- Luyten, J., and D. Roemmich, The 26-day oscillation in the equatorial Indian Ocean, unpublished manuscript.
- Madden, R. A., and P. R. Julian, Description of global-scale circulation cells in the tropics with a 40-50 day period, J. Atmos. Sci., 29, 1972.
- McCreary, J. P., and P. K. Kundu, A numerical investigation of the Somali Current during the Southwest Monsoon, J. Mar. Res., in press, 1988.
- Somali Current during the Southwest Monsoon, J. Mar. Res., in press, 1988.

- McCreary, J. P., Jr., S. R. Shetye, and P. K. Kundu, Thermohaline forcing of eastern boundary currents: with application to the circulation off the west coast of Australia, J. Mar. Res., 44, 71-92, 1986.
- McPhaden, M. J., Variability in the central equatorial Indian Ocean: I. Ocean dynamics, J. Mar. Res., 40, 157-176, 1982.
- Mertz, G. J., and L. A. Mysak, Evidence for a 40-60 day oscillation over the western Indian Ocean during 1976 and 1979, Mon. Wea. Rev., 112, 383-386, 1984.
- Molinari, R. L., J. F. Festa, and J. C. Swallow, Mixed layer and thermocline depth climatologies in the western Indian Ocean, NOAA Tech. Mem. ERL AMOL-64, 40 pp., Atlantic Oceanogr. and Meteorol. Lab., Miami, Florida, 1986.
- Moore, D. W., Rossby waves in ocean circulation, Deep-Sea Res., 10, 735-747, 1963.
- Moore, D. W., and S. G. H. Philander, Modeling of the tropical oceanic circulation, in The Sea: Ideas and Observations on Progress in the Study of the Seas, Vol. 6, edited by E. D. Goldberg, I. N. McCave, J. J. O'Brien, and J. h. Steele, pp. 319-361, John Wiley, New York, 1977.
- Mysak, L. A., and G. J. Mertz, A 40- to 60-day oscillation in the source region of the Somali Current during 1976, J. Geophys. Res., 89, 711-715, 1984.
- Nicholls, N., The Southern Oscillation and Indonesian sea surface Res., 89, 711-715, 1984.
- Nicholls, N., The Southern Oscillation and Indonesian sea surface temperatures, Mon. Wea. Rev., 112, 424-432, 1984.

- O'Brien, J. J., A. Busalacchi, and J. Kindle, Ocean models of El Niño, in Resource Management and Environmental Uncertainty, edited by M. H. Glantz and J. D. Thompson, pp. 159-212, John Wiley, New York, 1981.
- O'Brien, J. J., and H. E. Hurlburt, Equatorial jet in the Indian Ocean: Theory, Science, 184, 1075-1077, 1974.
- O'Neill, K., Equatorial velocity profiles: I. Meridional component, J. Phys. Oceanogr., 14, 1829-1841, 1984.
- Pedlosky, J., Geophysical Fluid Dynamics, 624 pp., Springer-Verlag, New York, 1987.
- Pickard, G. L., and W. J. Emery, Descriptive Physical Oceanography, 249 pp., Pergamon, New York, 1982.
- Piola, A. R., and A. L. Gordon, Pacific and Indian Ocean Upper Layer Salinity Budget, J. Phys. Oceanogr., 14, 747-753, 1984.
- Quadfasel, D. R., and J. C. Swallow, Evidence for 50-day period planetary waves in the South Equatorial Current of the Indian Ocean, Deep-Sea Res., 33, 1307-1312, 1986.
- Saetre, R., and A. J. da Silva, The circulation of the Mozambique Channel, Deep Sea Res., 31, 485-508, 1984.
- Schott, F., Monsoon response of the Somali Current and associated upwelling, Prog. Oceanogr., 12, 357-382, 1983.
- Schott, F., M. Fieux, J. Kindle, J. Swallow, and R. Zantopp, On currents and transports in the subtropical Indian Ocean east of Madagascar, J. Geophys. Res., in press, 1988.
- currents and transports in the subtropical Indian Ocean east of Madagascar, J. Geophys. Res., in press, 1988.

- Simmons, R. C., M. E. Luther, J. J. O'Brien, D. M. Legler,
Verification of a numerical ocean model of the Arabian Sea, to
appear in J. Geophys. Res.-Oceans, 1988.
- Soares, G. R., Contribution a l'etude de l'hydrologie et de la
circulation du Canal de Mozambique en hiver austral. These de
3eme cycle, Université de Paris VI, 89 pp., 1975.
- Sverdrup, H. U., Wind-driven currents in a baroclinic ocean; with
application to the equatorial currents of the eastern Pacific,
Proc. Nat. Acad. Sci., 33, 318-326, 1947.
- Swallow, J. C., and M. Fieux, Historical evidence for two gyres in
the Somali Current, J. Mar. Res., 40, Supplement, 747-755, 1982.
- Swallow, J. C., M. Fieux, and F. Schott, The boundary currents east
and north of Madagascar: I. Geostrophic currents and
transports, J. Geophys. Res., in press, 1988.
- Swallow, J. C., R. L. Molinari, J. G. Bruce, O. B. Brown, R. H.
Evans, Development of near-surface flow patterns and water mass
distribution in the Somali Basin in response to the southwest
monsoon of 1979, J. Phys. Oceanogr., 13, 1398-1415, 1983.
- Thompson, R.O.R.Y., Observations of the Leeuwin Current off western
Australia, J. Phys. Oceanogr., 14, 623-628, 1984.
- Wyrтки, K., Physical oceanography of the Southeast Asian waters,
Scientific Results of the Maritime Investigations of the South
China Sea and Gulf of Thailand 1959-1961, NAGA Rep. 2, 195 pp.,
Scripps Inst. of Oceanogr., La Jolla, Calif., 1961.
China Sea and Gulf of Thailand 1959-1961, NAGA Rep. 2, 195 pp.,
Scripps Inst. of Oceanogr., La Jolla, Calif., 1961.

Wyrтки, K., Oceanographic atlas of the International Indian Ocean Expedition, 531 pp., National Science Foundation, Washington, D.C., 1971.

Wyrтки, K., An equatorial jet in the Indian Ocean, Science, 181, 262-264, 1973.

Wyrтки, K., Indonesian through flow and the associated pressure gradient, J. Geophys. Res., 92, 12941-12946, 1987.

Wyrтки, K., Surface current charts for the Indian Ocean, unpublished manuscript.